Fuel 355 (2024) 129438

Contents lists available at ScienceDirect

Fuel

journal homepage: www.elsevier.com/locate/fuel

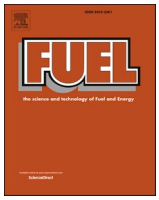

Full Length Article

Unconventional gasoline spray injection events: Compared evolution of experimental data and numerical simulations

Davide Viscione [a,*], Valerio Mariani [a,*], Stefania Falfari [a], Gian Marco Bianchi [a], Vittorio Ravaglioli [a], Giacomo Silvagni [a], Alessandro Montanaro [b], Luigi Allocca [b]

[a] DIN – Department of Industrial Engineering, Alma Mater Studiorum – University of Bologna, Bologna 40136, Italy
[b] Consiglio Nazionale delle Ricerche (CNR) – Istituto di Scienze e Tecnologie per l'Energia e la Mobilità Sostenibile (STEMS), Napoli 80125, Italy

ARTICLE INFO

Keywords:
Spray Mie Scattering technique
3D-CFD ultra high injection gasoline spray simulations
GCI injection pattern
Gasoline Common Rail injection

ABSTRACT

The current homologation standards in the automotive field impose the manufacturers to develop very efficient and clean engines. Low-Temperature Combustion engines have the potential to simultaneously reduce all the pollutants released while maintaining high efficiency. Among them, in Gasoline Compression Ignition (GCI) combustion technology, multiple injections allow to generate a tailored stratified charge which can auto ignite limiting the rough Pressure Rise Rate (PRR) and heat release rate typical of GCI. Therefore, the three-dimensional local distribution of the mixture becomes the key-point which the engine performance depends on. Due to emphasis on the multi-dimensional and local nature of the mixture formation phenomenon, three-dimensional CFD simulations are a promising and attractive method aiming at the design of the injection event features (timing, pattern, etc.). This paper deals with both experimental and CFD campaign on the evolution of a gasoline spray at ultra high-pressure multiple injection as well as high backpressure, typical of Gasoline Compression Ignition engines. The experimental tests have been conducted on a reference Diesel Common-Rail injector which shots in a constant-volume chamber. The hydraulic behaviour of the injector was characterized by means of the Bosch Tube principle whilst the Mie-scattering technique was used to capture the spray images. The numerical methodology is required to predict the Liquid Length Penetration and the jet morphology features (shape, area). Both experiments and simulations were conducted at different values of injection pressure (350, 500, 700 bar), back pressure (1–8 bar), energizing time (350, 600 μs), according to the operations of a real reference GCI test engine. Furthermore, a dedicated sub-model which takes into consideration the effect of the spray dynamics during the injection transient opening stage has been validated. The importance of this approach when dealing with short energizing time (e.g. 350 μs) is shown.

Comparing both the experimental and numerical results, the model has proven to efficiently reproduce the spray penetration and morphology features, also under the hypothesis of injector ballistic phase operations, whose determination is crucial in the early development and sustainability of such combustion concept.

1. Introduction

During the last decades, the development of new technologies in the automotive field was targeted to design engines with lower pollutant emissions and higher efficiency to be aligned with modern homologation standards. Together with the optimization of standard Spark-Ignition (SI) and Compression-Ignition (CI) engines ([1,2]), the modern research focused also on the development of new combustion concepts inside the cylinder, with the objective of combining both the benefits of SI and CI. In the current scenario, Low-Temperature Combustion (LTC) technologies are promising options to simultaneously obtain clean and efficient engines [3]. In fact, in LTC concepts, high efficiency is obtained by adopting high compression ratio and lean mixture, which are typical of Conventional Diesel Engines (CDE), while low pollutants are released in relation to the higher auto ignition time of gasoline compared to Diesel, allowing a more homogeneous air–fuel

* Corresponding authors.
E-mail addresses: davide.viscione2@unibo.it (D. Viscione), valerio.mariani4@unibo.it (V. Mariani), stefania.falfari@unibo.it (S. Falfari), gianmarco.bianchi@unibo.it (G.M. Bianchi), vittorio.ravaglioli2@unibo.it (V. Ravaglioli), giacomo.silvagni2@unibo.it (G. Silvagni), alessandro.montanaro@stems.cnr.it (A. Montanaro), luigi.allocca@stems.cnr.it (L. Allocca).

https://doi.org/10.1016/j.fuel.2023.129438
Received 14 March 2023; Received in revised form 5 July 2023; Accepted 4 August 2023
Available online 16 August 2023

Table 1
Main properties of commercial gasoline and Diesel fuel.

Property	Gasoline	Diesel fuel
Formula	C4 to C12	C10 to C15
Molecular weight (g/mol)	100–105	190–220
Carbon (%w)	85–88	84–87
Hydrogen (%w)	12–15	16–33
Density @15 °C (kg/m^3)	720–775	823–844
Viscosity @20 °C (mPa•s)	0.37–0.44	2.8–6.5
Boiling temperature (°C)	27–225	190–280

mixing, and consequently a reduced production of Particulate Matter (PM) and Nitrogen Oxides (NOx).

Although LTCs show good potential for the engine performance improvement, the main limitation for their adoption is the poor combustion phasing controllability and narrow operative range [4]. As a reference, in the baseline LTC, named Homogeneous Charge Compression Ignition (HCCI), a lean homogeneous mixture auto ignites almost simultaneously once the pressure and temperature inside the cylinder match the auto ignition threshold of the fuel. Thus, during combustion the heat is released according to complex chemical kinetics mechanisms, which are strongly influenced by the fluctuation of local mixture conditions [4].

To overcome the limitation of HCCI engines, the Gasoline Compression Ignition (GCI) relies on the injection of gasoline in multiple injection pulses in order to have a more robust control of the shape of the heat release during the combustion stage [5]. In particular, the first pulses allow to generate a local homogeneous mixture which auto ignites as for HCCI combustion, allowing to increase pressure and temperature inside the cylinder. Consequently, the fuel mass injected in last pulse experiences a reduced auto ignition delay, owing to a better combustion phasing controllability.

In this engine combustion configuration, the injection pattern becomes the main point for the achievement of a repeatable, efficient, and clean combustion for a given condition of pressure, temperature, and dilution degree inside the cylinder. In fact, the way the fuel distributes in the combustion chamber can completely define the nature of the combustion process. Several experimental and numerical studies available in the literature have been focused on the influence of the injection strategy and the stratification degree for pushing the limits of LTC combustion. Sjöber et al. conducted both experiments and chemical kinetics simulations in order to provide insights on the thermal and mixture stratification inside the cylinder of a test HCCI engine in order to smooth the PRR [6,7]. Dempsey et al. [8] presented a comprehensive analysis of the effect of different degrees of stratification (partial, moderate, heavy) GCI combustion by means of CFD simulations. The different degrees of stratification were realized by applying different injection split strategies (one premixed – one direct for the partial, three direct for the moderate, two direct for the heavy). The authors shown the comparison between advantages and shortcomings of each stratification degree in terms of emission of NOx, UHC, CO, PRR, combustion efficiency, indicated fuel consumption and noise, revealing the need of tailored analysis depending on the injector and chamber design. Other numerical works of worth on this topic are that by Atef et al. [9], where simulations were conducted for testing the effect of the nozzle geometry in a GCI reference engine (also a sweep of the Start of Injection (SOI) and of the fuel type were studied), and that by Priyadarshini et al. [10], where Large Eddy Simulations were performed in order to provide insights on the composition and thermal stratification in the case of double direct injection in a reference Diesel engine from the Sandia Laboratories. In [11] and [12] the authors (Agarwal et al., and Cung et al.) investigated the interaction between the pilot and the main injection events in GCI-operated engines by means of experiments, providing considerations on the effect of fuel stratification strategy on the low and high heat release phase of the combustion process. Currant et al. [13] conducted experimental tests on a medium duty Diesel engine to compare partial fuel stratification (at different injection timing and fuel mass split) and heavy stratification (at different injection timing). Both the stratification degrees showed the ability to achieve very low soot and NOx emissions under GCI conditions with different sensitivity to operating parameters such as injection timing and exhaust recirculated mass. The authors underlined the importance to perform numerical simulations in order to gain knowledge on the effect of the fuel spray-piston interaction.

Regarding the effect of the fuel chemistry, Park et al. [14] analysed the effect of the amount of gasoline blending in a CDE. Thanks to the reduced surface tension provided by increasing the amount of gasoline blending, smaller and more unstable droplets have been favoured. In addition, a longer ignition delay has been detected as gasoline percentage increased, owing to more homogeneous combustion and reduced PM and NOx emissions. Kim et al. [15] conducted tests to compare the Liquid Length Penetration (LLP) and spray cone angle of gasoline and Diesel injected by a Common-Rail system under both non-evaporating and evaporating conditions. Under non-evaporating conditions, no significant difference between the two fuels have been noticed, while the cone angle was slightly higher for gasoline spray. In the other hand, under evaporating conditions, gasoline spray halved the LLP compared to Diesel one. Similarly, Feng et al. [16] confirmed the results in [15] related to gasoline LLP with experiments adopting the Laser Induced Exciplex Fluorescence (LIEF). Instead, similar trends can be noticed in Vapour Length Penetration (VLP) for both fuels. Regarding the fuel dynamics inside the nozzle, Payri et al. [17] highlighted that the higher density of Diesel fuel leads to an higher mass flow rate with respect to gasoline one. Instead, the lower viscosity of gasoline fuel allows the needle to experience a quicker opening and closing phases. For the sake of comparison, Table 1 reports the main properties of both commercial gasoline and commercial Diesel fuel focusing on those that play a role in the injection process.

Together with the effect of different chemical properties of the injected fuel explained above, the injection pattern plays a fundamental role in the engine performance of a GCI concept, too. Sellnau et al. [18] performed a Design Of Experiment (DOE) to assess the optimal number of pulses, injection timing and pressure to maximise the fuel economy of a GCI engine running at 6 bar Indicated Mean Effective Pressure (IMEP) and 1500 rpm. Results showed that a triple injection strategy optimally phased allowed to increase of 8% the Indicated Thermal Efficiency (ITE) compared to the same obtained in CDE conditions. Moreover, with the same ITE compared to CDE combustion, a reduced NOx emission has been observed. Similarly, Wang et al. [19] and Zhang et al. [20] have shown that the injection phasing of the third injection and the ratio of the fuel injected mass significantly affect the combustion efficiency. In fact, if the injection phasing and the ratio of injected mass in multiple pulses events are incorrect, combustion efficiency is inhibited due to the inefficient fuel distribution inside the combustion chamber.

Several experimental campaigns have been conducted also at the test bench laboratory of the University of Bologna to investigate the performance of a CDE converted to operate in a GCI combustion mode, with promising results achieved in terms of pollutants reduction and efficiency improvement (further details can be found in [21]). As a reference, Stola et al. ([22,23]) conducted several campaigns to investigate the influence of the ignition delay of a Research Octane Number (RON) 95 gasoline fuel injected using a Common-Rail system in different injection and in-cylinder conditions. Again, the obtained results demonstrate that the injection pressure is a key factor for combustion optimization and for the limitation of combustion impulsiveness. Furthermore, the Start Of Combustion (SOC) provided by the auto ignition of the first injections significantly affect the remaining combustion stability and repeatability. Consequently, with the objective to analyse the Rate of Heat Release (RoHR) shape in relation to the adopted injection pattern, dedicated three dimensional (3D) Computational Fluid Dynamics (CFD) simulations are worth to be implemented ([24,25,26]). In this context, in order to take into account the effect of the different chemical characteristics of the fuel and different injection

Table 2
Injector geometrical characteristics.

Injector Name	MJII Common Rail
Number of nozzles	7
Outlet nozzle geometric diameter (d_0), [μm]	121
Length of the nozzle hole, [μm]	750
Conicity (*ks-hole)*	1.3
Cone angle [deg]	75

pattern in the generation of a stratified gasoline-air mixture in a CDE operating with GCI mode, a dedicated code must be developed and implemented in 3D-CFD simulations. The goal is to reasonably represent the real in-cylinder conditions facing the combustion process. Since, during the experiments [21-23], the first two injections (Pilot and Pre) are characterized by a low Energizing Time (ET) and ultra-high pressure (350μ s at pressures of 300, 500 and 700 bar), they belong to the ballistic phase operation of the injector [27]. Under this hypothesis, to better represent the current injection pattern, it is mandatory to consider also the fuel dynamics inside the injector hole, which directly affects the discharge coefficient (C_d) of the orifice.

Several works have presented an overview of the variation of the discharge coefficient during the transient phase on the injector needle lift. Payri et al. ([28,29]) analysed the effect of the partial needle lift on the overall discharge coefficient of a Common-Rail injector. Results showed that both the mass flow and spray momentum flux depend also on the instantaneous needle lift. Moreover, the numerical simulation allowed to calculate the real needle lift during the experiments, too, comparing the values of the upstream pressure. Similarly, other studies can be found in the literature with the same conclusions ([30,31,32,33,34]).

Since the adoption of a different fuel and different injection pattern significantly affect the overall RoHR shape of a CDE running in GCI mode, a tailored 3D-CFD simulation methodology is needed in order to capture the local mixture composition and distribution must be performed. In this context, the combined effect of ultra-high pressures even for very short ETs significantly influences the evolution of a gasoline fuel spray injected by a Common Rail system. Yamaguchi et al. [35] analysed the gasoline spray characteristics of different Common Rail injector nozzle geometries. Spray imaging techniques and flow rate measurements of a fixed fuel injected mass of 27 mg have been implemented to extract data which might be used to tune 3D-CFD codes. However, regarding the specific spray pattern adopted during GCI operations of interests, the injected mass is much lower. Moreover, no comparisons between simulated spray plumes can be noticed. Similarly, Feng et al. [16] and Payri et al. [36] investigated the spray development of a gasoline fuel injected in a Common Rail system adopting an ET longer than 1 ms, well above the one adopted during Pilot and Pre injection events of interests (350μ s). Hence, the specific application has been scarcely investigated in the literature.

In light of the above literature review, it is clear that when GCI combustion is concerned, a tailored numerical methodology is a key to capture the spray behaviour and the fuel distribution in order to provide insights and guidelines on the injection strategy effects and optimization. In the present work, three-dimensional CFD simulations have been implemented for reproducing experimental tests conducted on a specific Common Rail injector which is installed in a GCI-operated CDE at the test bench of the University of Bologna. The experimental spray characterization has been conducted at the STEMS-CNR laboratories in Naples adopting the Mie-Scattering technique to capture the LLP and cone angle of a gasoline spray injected under non-evaporating conditions in a quiescent constant-volume vessel by a Common-Rail system at various ET, injection pressure and back pressure. CFD simulations have been set by choosing carefully the features of the computational grid and the Lagrangian sub-models in order to ensure the accuracy and reliability of the method with respect to the experiments. In particular, emphasis has been placed on the effect of the nozzle transient opening phase on spray breakup and penetration by implementing an ad hoc variable-discharge coefficient simulation strategy. Despite the fact that a number of works have yet presented the effect of injection pressure values above 500 bar and backpressure values above the ambient one, the behaviour of both real and simulated high pressure gasoline spray during short energizing time injection events (350 μs) has been scarcely investigated. Under those conditions, the transient opening stage has a strong impact on the injection event compared to the steady flow rate phase. This focus has high relevance considering the role of the free spray during pre-injection events (which are operated at short energizing time) on the mixture preparation.

Considering the extreme sensitivity of the GCI combustion to the mixing process, together with the lack of in-cylinder optical analyses not available in every-day facilities, this work aims at enhancing the knowledge on gasoline spray injected at non-conventional conditions, in particular high injection pressure and low energizing time. This can be worth in the perspective of adding bricks to the state of the art in a framework in which, as it is known in the literature ([11,13]), there are not generally valid rules. Thus, specific injection configurations should be reproduced to determine the proper guidelines and to optimize the final engine configuration. The results shown that the methodology can match the time evolution of the LLP as well as the plume area and morphology, thus, reliable predictions of the local fuel distribution and of the mixing phase can be expected.

2. Experimental campaign

This section describes the experimental setup adopted to measure the mass flow rate and to capture the spray morphology in the case of gasoline injected with a high-pressure Common Rail system. The experimental activity has been structured in order to follow the typical operative points covered by the Common Rail injection system during the GCI mode [21]. The GCI arrangement was adopted using a solenoid injector with symmetric seven-hole nozzle of automotive origin, previously used during the experiments at the test bench, whose characteristics are listed in Table 2.

The injector ETs used during the flow rate acquisitions have been selected referring to the typical ones adopted during the multiple injections operations. Similarly, the back pressure imposed in the vessel facing the injector followed the typical values of the in-cylinder pressure at the correspondent Start Of Injection (SOI).

2.1. Experimental methodology

The experimental activities concerning the fuel behaviour for GCI applications have been carried out both in terms of instantaneous fuel injection rates and spatial–temporal evolutions of the jets at the defined operating conditions. A Common Rail injection apparatus for Diesel engines has been utilized to feed an engine multi-hole electro-injector using commercial gasoline RON 95 fuel, which has been properly mixed with traces of lubricant fluid in order to avoid system damages due to grip while preserving the original properties of the injected fuel. A home-made Programmable Electronic Unit (PECU) managed the injection system, by a remote-control computer, enabling to set injection strategies and adapt the explored control parameters (timing).

2.1.1. Injector characterization apparatus

The dynamic characterization of the fuel delivered by the injector has been pursued in terms of instantaneous and total injected mass for different injection pressures and different ET both for single and double (Pilot + Main) strategies and, for the last, at various Dwell Time (DT). An AVL Injection Rate Meter has been used to measure the injected mass; it works on the “Bosch pipeline” principle [37]. The device is reported in Fig. 1.

The increase of the pressure in the cockpit, produced by the injected

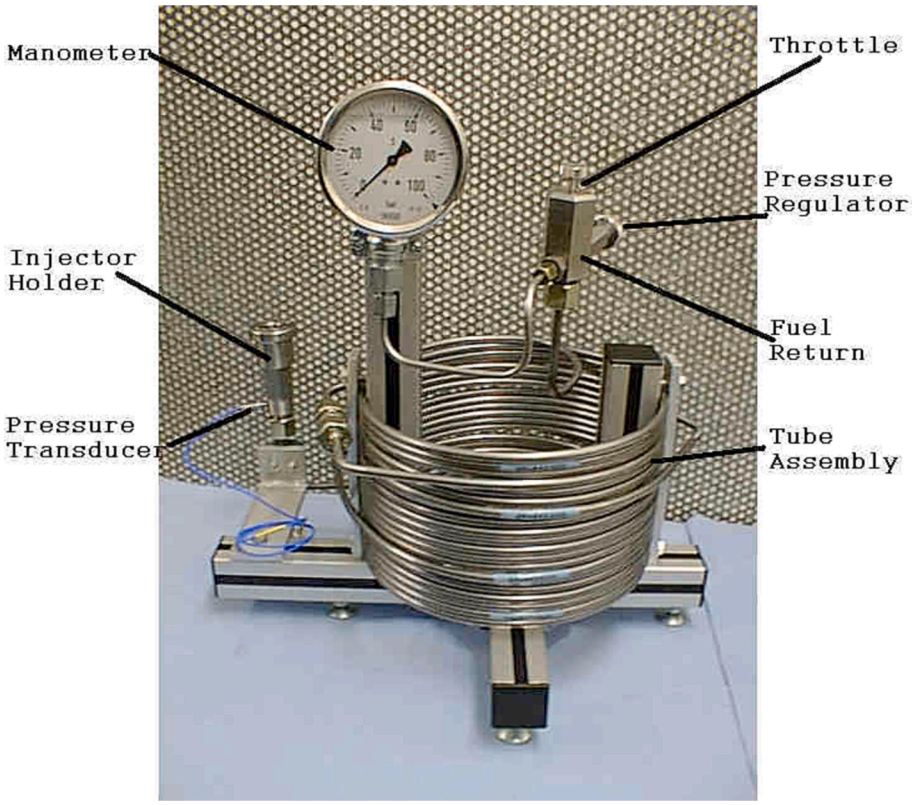

Fig. 1. Fuel injection meter for instantaneous and total flow rate measurements.

Table 3
Definition of the test conditions to obtain the instantaneous flow rate curves.

Energizing Time [μs]	Injection Pressure [bar]
350	350
	500
	700
600	350
	500
	700

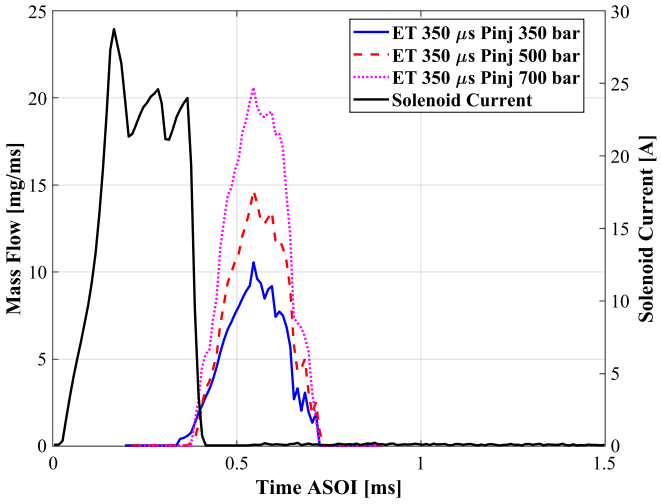

Fig. 2. Mass flow rate in the ballistic phase.

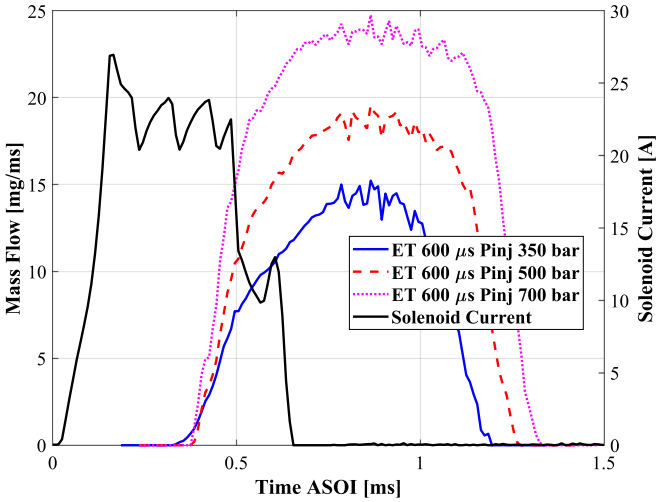

Fig. 3. Mass flow rate in the repeatable phase.

fuel at the "injector holder" location, is registered by a GMD12D – AVL piezoquartz transducer, once the pressure in the pipe reached a constant value to avoid cavitation interferences, around 5.0 MPa fixed by a regulator at the pipe end. Then, this measured pressure increase has been transformed in fuel rate trough the chemical-physical properties of the fluid and the geometrical parameters of the tube. The time resolution of the fuel rate is related to the frequency bandpass of the sensor and the sensitivity of the acquisition devices used and can be less than 1μ s. A time step of 5μ s has been adopted in our setup. The instantaneous injected quantity $\dot{q}(t)$ is derived by the Eq. (1):

$$\dot{q}(t) = \frac{\Delta p_{gauge} A_{tube}}{a\rho} * 10^5 \left[\frac{mm^3}{s}\right] \quad (1)$$

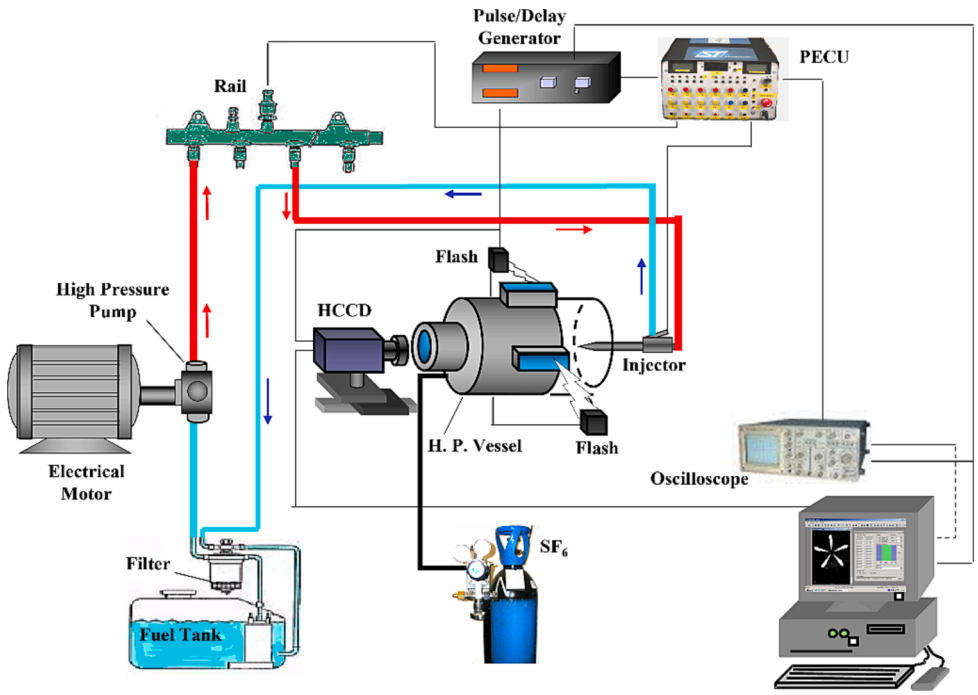

Fig. 4. Mie-scattering experimental layout to visualize the gasoline sprays.

Table 4
Mie-Scattering tests conditions.

ET [μs]	Injection Pressure [bar]	Back Pressure [bar]			Vessel temperature [K]
350	350	1.67	5	8.4	298
	500	1.67	5	8.4	
	700	1.67	5	8.4	
600	350	1.67	5	8.4	
	500	1.67	5	8.4	
	700	1.67	5	8.4	

where the Δp_{gauge} is the instantaneous increasing piezo transducer data, A_{tube} the (constant) section of the pipe, a the sound speed in the fluid, and ρ the density of the fluid (gasoline). Finally, the total amount of injected fuel calculated by Equation (1) over the entire ET has been compared with that collected at the pipeline exit of the Bosch tube and weight by a precision balance. Further details of the used methodology are reported in [38] while clarifications on the test conditions can be found in Table 3.

Fig. 2 shows the behaviour of the mass flow rate in the case of an ET = 350μs for different injection pressures. In those conditions the mass flow rate cannot reach a plateau value, since the injector needle has not enough time to reach its maximum lift. Given the different injection pressures adopted, the opening and closing phases experience a different derivative. This is reflected in a different effective opening time, too: the lower is the pressure, the longer will be the closing phase.

Regarding the behaviour of the mass flow rate outside the ballistic phase, Fig. 3 highlights the curves adopting an ET = 600μs. It can be noticed that the time needed by the mass flow rate to reach the stable value is almost the same in the three conditions (the transient range is about 350 −400μs). Conversely, for the same ET applied to the injector coil, the higher is the pressure, the longer will be the effective opening time.

The curves of mass flow rate presented above will be used to estimate the effective diameter of the droplets to impose in the 3D-CFD code. The next section will briefly describe the theoretical background and the results related to the actual topic.

2.1.2. Spray optical characterization facility

The measurements of the spatial and temporal evolutions of the spray plumes, emerging from the injector nozzle, have been carried out in an optically accessible, constant-volume combustion vessel filled by inert gas kept at engine-like pressures. The pressurized chamber hosted the injector spraying the gasoline at pressures varying between 35 and 70 MPa and having equivalent backpressures up to 5.0 MPa. To fulfil safe conditions, a high density gas, SF6 ($\rho = 6.2 kg/m^3$), has been used for reaching the highest desired densities in the vessel.

The Mie-scattering optical technique has been applied to characterize the liquid fuel evolving in the chamber. A high-power flash lamp, operating in visible wavelength and at its plateau intensity, was synchronized with the injection command lighting up the gasoline droplets in the spreading phase after being injected. Images of frozen plumes have been collected by a high-speed CMOS camera, also synchronized with the event. A Photron FASTCAM SA4 camera has been employed with different lens configurations realizing diverse time resolutions: a 92 mm focal length, at 30 and 50 kg/m^3 of vessel gas density, achieving 12,000 fps and corresponding to a time resolution of 83.3μ s, while, at 10 kg/m^3, a 25 mm focal length permitted 22,500 fps equivalent to a time step of 44.4μ s. Five consecutive repetitions per each condition have been carried out to permit a spread distribution analysis of the measured data and to furnish an error bar for each measurement point. A sketch of the optical setup is reported in Fig. 4 were the orthogonal configuration of the Mie-scattering shows the enlightened fuel plumes coming from the injector (at the top of the vessel) being captured by the high-speed camera. The vessel optical accesses were windows of quartz, 80 mm in diameter, enabling the record most of the liquid fuel during its evolution. Additional references for measurements of the evolving liquid phase are reported in [39].

The captured images of the spray evolution have been processed offline by a homemade software that, subtracting the frame background, filtering the jet figures, and determining their edges, extracted the plumes contours enabling, in an iterative mode, the measurements of the parameters of interest. More details on the processing procedure are collected in [40]. Spray tip penetrations, defined as the maximum distance from the nozzle at which it was possible to find most of the detected fuel, have been measured vs time from the start of injection,

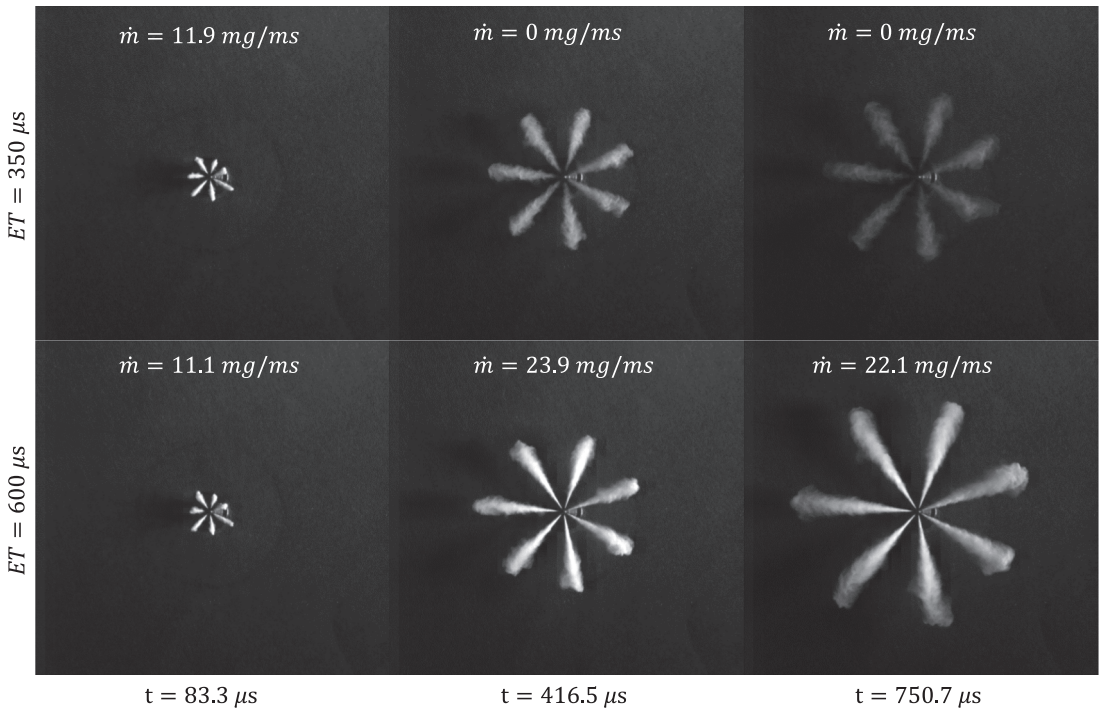

Fig. 5. Evolution the spray plumes for an injection pressure of 700 bar and a back pressure equivalent of 8.4 bar for two ET.

Table 5
Test conditions during the validation procedure.

ET [μs]	Injection Pressure [bar]	Back Pressure [bar]		Vessel temperature [K]
350	350	5.0	8.4	298
	500	5.0	8.4	
	700	5.0	8.4	
600	350	5.0	8.4	
	500	5.0	8.4	
	700	5.0	8.4	

averaged both on the seven spray plumes and on the five iterations. The spray-cone angle, defined as the angle between the external tangents to the surface of the jet, measured at the middle of its penetration for the fully developed jet, was the other main parameter of interest, averaged on the seven plumes and the five repetitions, too. Regarding the operative points covered during the acquisition of the spray morphology, Table 4 highlights the main characteristics.

The images of the experimental evolution of the spray obtained with the Mie-Scattering technique will be used as a comparison with the same obtained during the 3D-CFD simulations. In particular, LLP, projected spray plume area and plume morphology are the key points for the comparison. The high-frequency images have been acquired in two different values of ET while varying both the injection pressure and the back pressure. The test conditions are the same of the ones listed in Table 4.

The imposed back pressure has been obtained with the adoption of Sulphur Hexafluoride SF6 inside the constant volume vessel. Hence, the spray would face a gas density which is equivalent to have air at a pressure of almost 8, 25 and 42 bar, respectively, which are typical values that the injector would face during in-cylinder operations once multiple late injections are implemented. Considering that the Pilot and Pre injections are performed during the late phase of the compression stroke and the Main one around the Top Dead Centre (TDC), the validation has been performed considering the last two higher back pressures, since their values are similar to the ones the injector is faced with in real conditions.

Fig. 5 compares the evolution of the spray plumes at three consecutive times after Start Of Injection (aSOI) in the case of ET $= 350\mu s$(top) and ET $= 600\mu s$ (bottom) for an injection pressure of 700 bar and a back pressure of 8.4 bar. During the early opening stage (t $= 83.3\mu s$), a strong anisotropy between the plumes is highlighted. This will be reflected also in a high deviation of the LLP of each single plume with respect to its mean value. At this stage, the effect of the ET is limited due to the fact that the two jets feature almost the same mass flow rate, indeed, they are similar both in terms of intensity and shape. In the last two times aSOI selected, the anisotropy of the plumes is limited. Despite the fact that the two jets have almost the same overall shape, their intensity is different because of the instantaneous mass flow rate, indeed at ET $= 350\mu s$ the jets are not fed by new fuel anymore whilst at ET $= 600\mu s$ the injection event is ongoing. The morphology of the splay plumes in all the remaining different conditions can be seen in the Appendix B at the end of the current manuscript, compared with the simulated ones. For the latter comparison, considering that, for a fully developed flow rate, the morphology of the experimental plumes is almost the same, just one single plume has been used for the comparison.

Regarding the experimental LLP, it will be discussed during the next sections as a comparison with the same obtained during the 3D-CFD simulations.

3. 3-D CFD SIMULATIONS

In this section, the computational methodology is presented, the goal being to have a robust evaluation of the evolution of a gasoline spray injected using a high-pressure Common Rail system. Firstly, a theoretical background on theory behind the discharge coefficient determination is discussed. Then, the computational setup is presented also focusing on the algorithms used for the determination of the LLP, projected spray plume area and morphology. Regarding the points covered during the simulations, Table 5 summarizes the test conditions.

3.1. Theoretical background

The mass flow rate can be defined as (Eq. (2)):

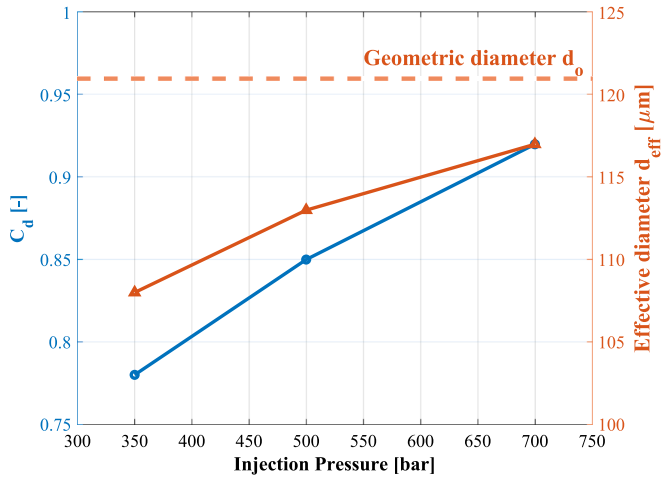

Fig. 6. Discharge coefficient and effective diameter according to the actual injection pressure.

$$\dot{m}_f = \int_{A_0} \rho u dA \left[\frac{kg}{s}\right] \tag{2}$$

where A_0 represents the geometric area of the hole, ρ and u the density and velocity at the hole exit. To simplify this complex flow configuration, it is assumed that the injected fuel is fully in the liquid phase flowing through an effective area A_{eff} with an effective velocity u_{eff}. At this point, it is useful to relate the effective mass flow rate with the theoretical one by non-dimensional coefficients. As stated by the Bernoulli's equation applied between the inlet and the outlet of the nozzle hole, it is possible to calculate the theoretical velocity as $u_{th} = \sqrt{2\Delta p/\rho}$, where Δp represents the pressure difference between inlet and outlet of the nozzle hole. It is now possible to calculate the non-dimensional discharge coefficient C_d (Eq. (3)) to relate the geometric area A_0 and theoretical velocity u_{th} with the real mass flow rate.

$$C_d = \frac{\dot{m}_f}{\rho u_{th} A_0} [-] \tag{3}$$

The discharge coefficient accounts for the loss of velocity due to frictions and loss of flowing area with respect to the geometric size due to phase change and vena contract phenomena. Consequently, the discharge coefficient can be expressed as the product by two different coefficients which account for the two above mentioned effects respectively (Eq. (4)):

$$C_d = C_v C_c [-] \tag{4}$$

where the area contraction coefficient C_c considers the restriction of the nozzle area A_0 (Eq. (5)), while the velocity reduction coefficient C_v includes the velocity losses (Eq. (6)):

$$C_c = \frac{A_{eff}}{A_0} = \frac{d_{eff}^2}{d_0^2} [-] \tag{5}$$

being d_{eff} and d_0 the effective and geometric diameters, respectively.

$$C_v = \frac{u_{eff}}{u_{th}} [-] \tag{6}$$

At this stage, the flow rate curves of Fig. 2 and Fig. 3 are beneficial to define the droplet diameter at the nozzle outlet. In order to be defined, the Equation (3) is applied using the mass flow rate during the steady-state phase of Fig. 3. In addition, an estimation of the C_v must be performed. As shown in Fig. 6, applying Equation (3) using the geometric diameter d_0 and the pressure difference at the nozzle boundaries, C_d can be calculated.

For those kinds of injectors, the pressure-to-velocity conversion is very efficient [41]. Thus, considering the calculated values for the C_d shown in Fig. 6, a $C_v = 0.98$ might be a reasonable value.

3.2. Lagrangian multi-phase models

In this work, the droplet initialization subroutine introduces liquid fuel in the computational domain as primary parcels (*blobs*, representative of a group of droplets) following a modified version of the Hug & Gosman atomization model. Velocity and cone angle are imposed referring to the experiments conducted at the STEMS-CNR Lab, while the diameter of the injected parcels is set according to the previously shown in Fig. 6.

Once droplets are introduced into the computational domain, they may become unstable mainly due to the action of the drag forces induced by their motion relative to the continuous phase. The rate of the breakup process is defined as in Eq. (7):

$$\frac{dD_d}{dt} = \frac{D_d - D_{d,stable}}{\tau_d} \left[\frac{m}{s}\right] \tag{7}$$

where D_d is the instantaneous droplet diameter, $D_{d,stable}$ the stable droplet diameter and τ_d the characteristic time scale.

For the adopted breakup model, the Reitz-Diwakar one [42], the process occurs in two modes:

- Bag breakup, for which the droplet is disintegrated once the surface tension forces are overcome due to the non-uniform pressure field around it;
- Stripping breakup, for which the liquid is sheared or stripped from the surface of the droplet.

For both the two modes, the instability is determined by the value of the Weber Number (Eq. (8)):

$$We = \frac{\rho |\boldsymbol{u} - \boldsymbol{u}_d|^2 D_d}{2\sigma_d} [-] \tag{8}$$

where ρ is the gas density, D_d the instantaneous droplet diameter and σ_d is the surface tension coefficient. In particular, the bag breakup process occurs if $We \geq C_{b1} = 6$, while the stripping one if $\frac{We}{\sqrt{Re_d}} \geq C_{s1} = 0.5$ (Re_d the droplet Reynolds number). The $D_{s,stable}$ for each regime is the one which satisfies the equality in the above equations. Similarly, also the characteristic time scale is computed differently for the two modes according to Eq. (9) and Eq. (10), respectively:

$$\tau_{b,bag} = \frac{C_{b2} \rho^{1/2} D_d^{3/2}}{4\sigma_d^{1/2}} [s] \tag{9}$$

$$\tau_{b,stripping} = \frac{C_{s2}}{2} \left(\frac{\rho_d}{\rho}\right)^{1/2} \frac{D_d}{|\boldsymbol{u} - \boldsymbol{u}_d|} [s] \tag{10}$$

Where ρ_d is the droplet density, $C_{b2} = \pi$ and $C_{s2} = 20$.

3.3. Computational setup

As introduced earlier, the computational setup has been developed considering the simulation of the injection of a single plume, owing to a reduction on the cost of the computational time. This choice does not limit the general validity of the simulations as far as the droplet–droplet collision modelling is not taken into account in standard spray simulation. Consequently, the overall mass flow rate has been divided by the number of nozzle holes. The comparison with the experimental data will be carried out considering the mean value and the maximum and minimum values of the LLP for each test.

The commercial software used for the simulation was STAR-CD 4.22 by Siemens. The computational domain was modelled as a squared-section box of size 60 × 30 × 40 mm.

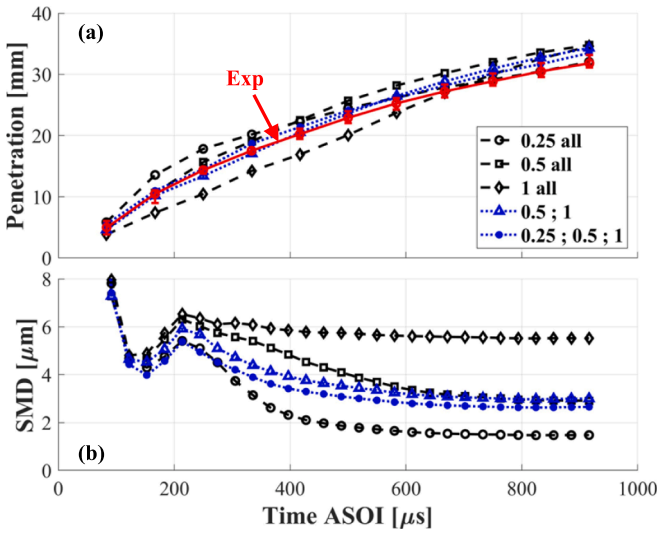

Fig. 7. Comparison of the LLP according to the grid resolution.

Each face of the computational domain has been treated as an adiabatic wall at fixed temperature, thus, the overall box dimensions have been imposed to prevent the interaction between spray momentum and the walls.

It is remembered that the coupled Eulerian-Lagrangian approach requires that the combination of the droplet size and of the cell size fulfil the hypothesis of particles dispersed in the continuum phase. Furthermore, the grid size should be consistent with both the spatial scale of the breakup phenomenon and the typical cell size then used in engine simulations, resulting in a complex compromise. Fig. 7 compares the LLP (Fig. 7(a)) and the Sauter mean diameter (SMD, Fig. 7(b)) obtained with different grid resolutions. The black lines in the legend represent the base grid size of 0.25 mm, 0.5 mm, and 1 mm with no local refinement. The blue lines represent base gride size of 1 mm with two different local refinements along the breakup region, namely a single refinement of 0.50 mm and a two-steps refinement 0.5 mm-0.25 mm in the same region.

It can be observed that, as expected for gas flow simulations with a dispersed phase, the grid size significantly affects the results due to the struggle in accurately modelling the gas–liquid mass and momentum coupling without violating the underling dispersed phase assumption. Focusing on the very early penetration length (5–10 mm), for the black curves (no local refinements) the finer is the grid, the larger is the penetration due to the anticipated breakup onset and the lower aerodynamic resistance (smaller surface of the droplet, (Fig. 7(b)). In this range, both the grids with local refinement along the breakup length (blue curves) lie on the 0.5 mm grid, which is in a good agreement with the experimental data. In the time range associated to very early penetration length the curves of the locally refined grids lie on the black curves associated to the corresponding base size (i.e., 0.5 and 0.25 mm). Fig. 7(a) shows that a coarser grid in the fully developed spray (beyond 20 mm downstream the nozzle tip, smallest diameter and velocity values) helps to capture the penetration curve after the slope change. Despite the slight differences between the results returned by the two grids featured with the local refinement, the one with two refinement steps has been chosen because of the better match against experiments without significant additional computing time.

Fig. 8 highlights the geometry of the computational grid and of the related refinements. Around the injection point, two refinement levels have been implemented to capture the primary break-up and the primary-secondary breakup transition spray processes. The minimum cell size of 0.25 mm has been chosen in order to avoid the violation of

Table 6
Geometric characteristics of the computational grid.

Base grid size [mm]	1.00
Refinement first level [mm]	0.50
Length of the first level refinement [mm]	10
Refinement second level [mm]	0.25
Length of the second level refinement [mm]	5
Number of cells [-]	128,000

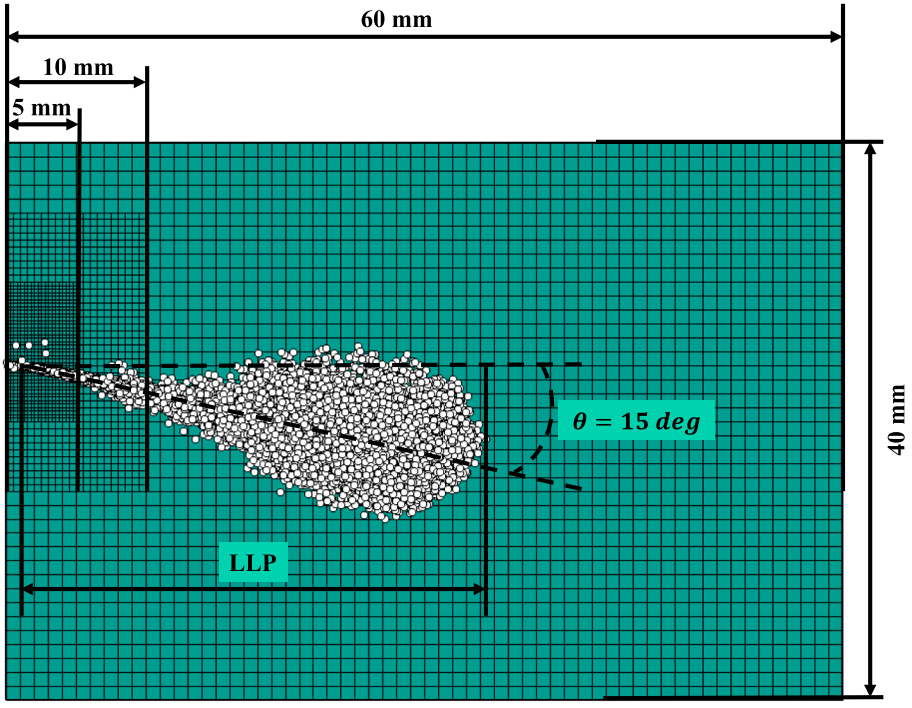

Fig. 8. Visualization of the computational grid and refinements.

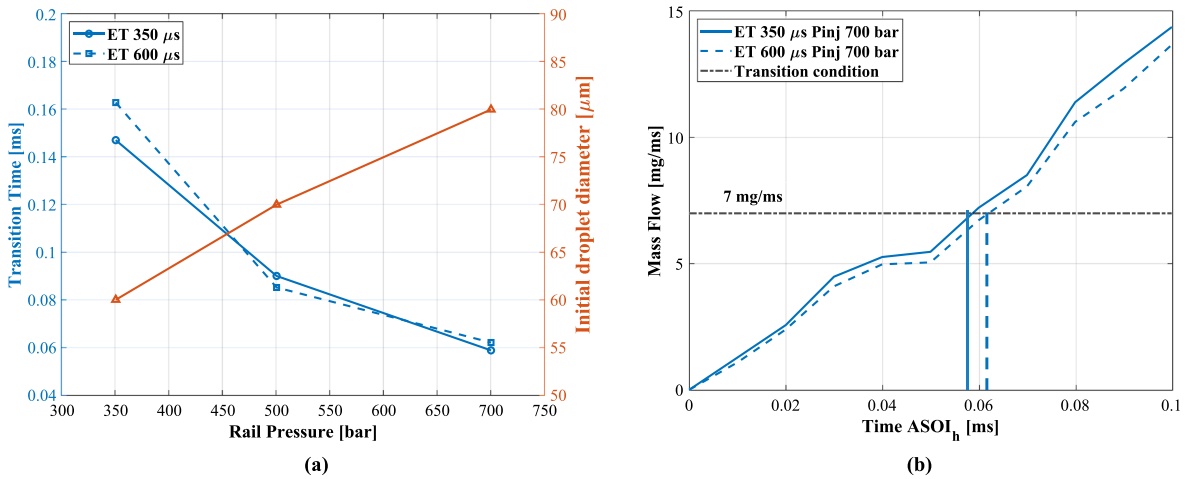

Fig. 9. Transition time and initial droplet diameter according to the actual injection pressure (a); Comparison between the flowrates obtained with the injection pressure of 700 bar during the opening phase (b).

the hypothesis of dispersed phase on the liquid droplets approached with the Lagrangian method. A base grid side of 1 mm has been set according to the typical size adopted in simulations regarding the Internal Combustion Engine (ICE). The base size fines up to 0.25 mm by halving the grid size two times towards the injector tip point location according to the steps shown in Fig. 8. Table 6 summarizes the geometric characteristics of the computational domain.

Both the liquid and the vapor phase of the fuel were selected from the STAR-CD built-in NIST database as a pseudo-pure fluid representing the chemical characteristics of the commercial RON 95 gasoline. Reynolds Averaged Navier Stokes (RANS) approach has been adopted, with the $k-\epsilon$ eddy viscosity two equations to model the turbulence.

The selected solution algorithm was the Pressure-Implicit with Splitting Operators (PISO). Regarding the differencing schemes, a second order Central-Differencing (CD) method has been selected for momentum, pressure, temperature, and density. A fixed time step of 1 μs has been imposed according to the time scale of the break-up process.

Once the models and geometric characteristics of the computational domain have been defined, the next section is meant to describe the methodology aimed at the implementation of the variable C_d during the 3D-CFD simulations.

3.4. Variable discharge coefficient modelling

As discussed earlier, the implementation of a different discharge coefficient during the opening stage on the needle lift follows the necessity to consider also the transient dynamics of the injected fuel. In fact, since the mass flow rates the code must follow during the simulation are the same of Fig. 2 and Fig. 3, the LLP would be underestimated with respect to the experimental one if the droplets are introduced with their diameter calculated by Equation (6). This is given by the higher drag deceleration force the droplet would be subjected to. Consequently, a reduced diameter must be imposed during the transient stage.

In order to properly define such phenomenon, two quantities must be defined:

- Transition time between the C_d adopted during the transient and the steady-state;
- Initial diameter of the injected droplets during the transient stage.

With regards to the former aspect, combining the data of needle lift in [41] with the trend of C_d reported in [28], the literature reports that the achievement of the steady discharge coefficients might occur even before the end of the opening stage. An iterative procedure has been performed to tune both the transition time and the diameter of the injected droplets during the transient stage. In particular, the best transition condition to match the experimental LLP during the early stages corresponds to the instant at which the mass flow rate reaches a value of 7 mg/ms. Given the different shape of the mass flow rates, the transition time will be higher for lower injection pressures, since the derivative of the opening stage curve is lower. The initial diameter of the droplets is estimated considering the trend of discharge coefficients in [28], reported considering the actual value of the nozzle diameter d_0. Fig. 9(a) reports both the trends of the transition time and initial droplet diameter according to the actual injection pressure.

As reported by Fig. 9(a), the transition time slightly changes depending on the ET. This is due to the slight difference between the shape of the mass flow rate profiles, highlighted in detail in Fig. 9(b) regarding the condition of injection pressure of 700 bar and ET of 600 μs. In particular, the curves shown in Fig. 9(b) start after the hydraulic SOI ($aSOI_h$). After the transition time, the initial droplet diameter switches between the values reported in Fig. 9(a) and the ones showed in Fig. 6, namely from 60 μm to 107 μm at 350 bar, from 70 μm to 113 μm at 500 bar, from 80 μm to 117 μm at 700 bar.

The variable discharge coefficient methodology with the above-mentioned values is implemented in all the simulation results shown in the next sections. In order to validate it, a comparison of LLP, spray morphology and area between simulations and experiments will be carried out.

3.5. LLP and projected spray plume area calculation

As highlighted in Fig. 8, the LLP calculation of the simulated cases follows the same approach adopted during the experiments. In fact, the LLP is obtained computing the distance between the farthermost droplet and the injector tip. The resulting measurement is converted in millimetres knowing the image resolution in terms of pixel/mm. Consequently, the calculated quantity is the radial LLP, while the real one can be computed knowing the actual spray angle ($\theta = 15$ deg in Fig. 7). However, the following figures showing the computing LLP refer to the radial one.

Similarly, the projected spray plume area is calculated computing the number of pixels representing the spray plume. Then, knowing the image resolution, the area of a single pixel is converted in mm^2 and the whole projected spray plume area is calculated multiplying the number of pixels with the area of a single one.

4. Results

The current section is meant to highlight the results obtained

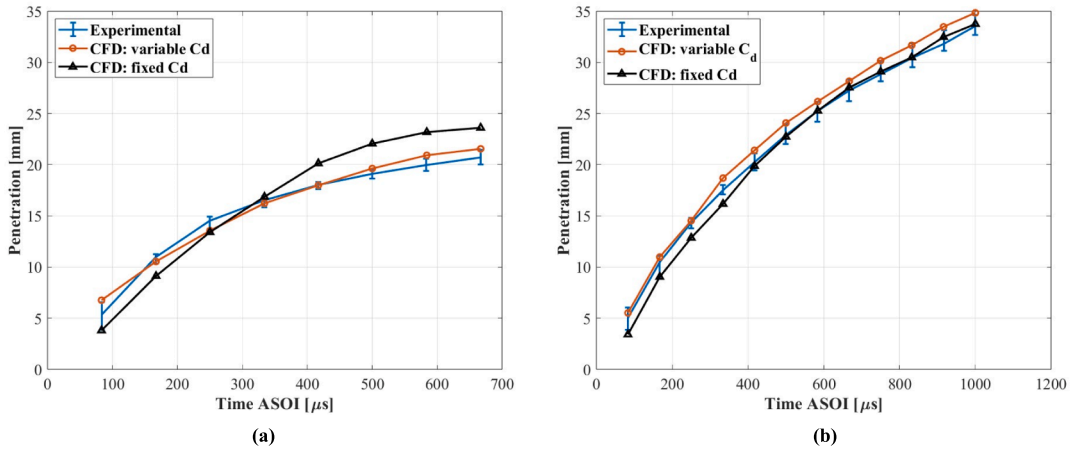

Fig. 10. Comparison of LLP between experimental and simulated tests for an ET = 350 (a) and for an ET = 600 (b) at the injection pressure of 700 bar and a back pressure of 8.4 bar.μsμs.

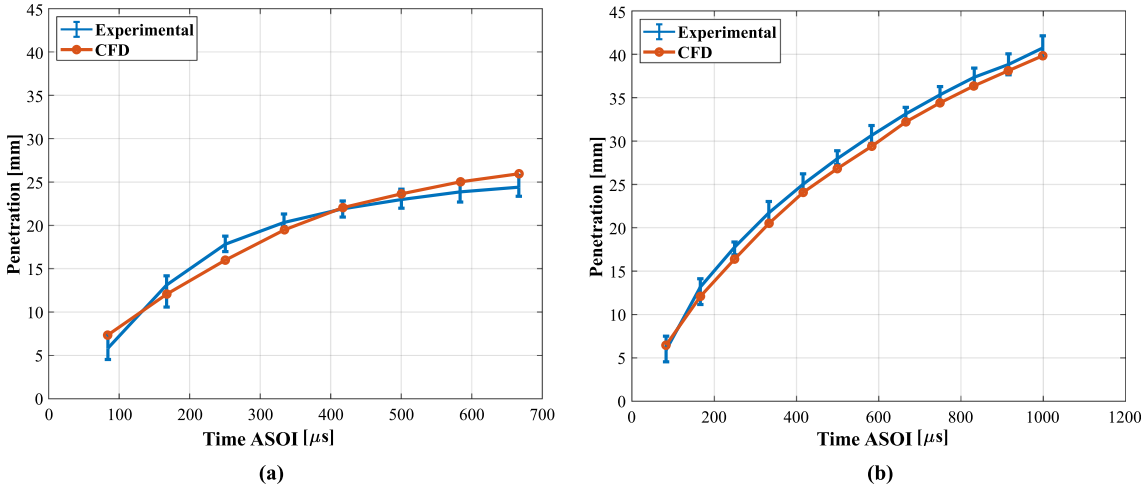

Fig. 11. Comparison of LLP between experimental and simulated tests for ET = 350 μs (a) and ET = 600 μs (b) for the injection pressure of 700 bar and the back pressure of 5 bar.

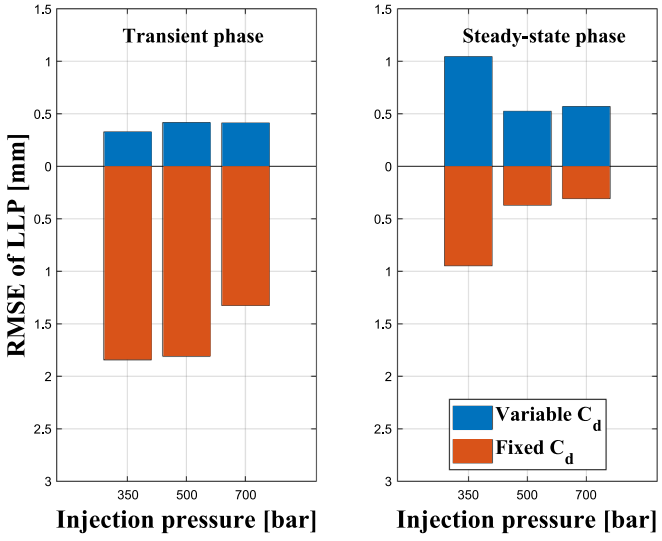

Fig. 12. Comparison of RMSE of LLP for all the tested conditions (Back pressure 8.4 bar).

adopting a variable C_d during the 3D-CFD simulations, comparing them with the experimental data. The experimental points covered during the validation procedure follows the ones listed in Table 5.

4.1. Liquid Length penetration

Fig. 10 compares the values for the LLP obtained during the experiments and the simulations for two different ET applied (350 μs in (a) and 600 μs in (b)) in the case of an injection pressure of 700 bar and a back pressure of 8.4 bar.

A variable C_d allows to reduce the error between the experimental and simulated LLP calculations. In particular, a fixed $C_d = 0.92$ (calculated with Equation (3) and shown in Fig. 6) underestimates the simulated LLP during the early spray development. In the contrary, for the low ET = 350 μs (Fig. 10(a)), the simulated spray with fixed C_d has a higher protrusion with respect to the experimental one during the late phase. For an ET = 600 μs (Fig. 10(b)), the prediction of the spray behaviour improves especially during the early spray development, while the two trends of LLP with fixed and variable C_d almost overlap during the steady-state phase. This is likely given by the consideration that, during the latter phase, both the models inject droplets with the same diameter.

Considering the benefits the variable C_d provided to the prediction of

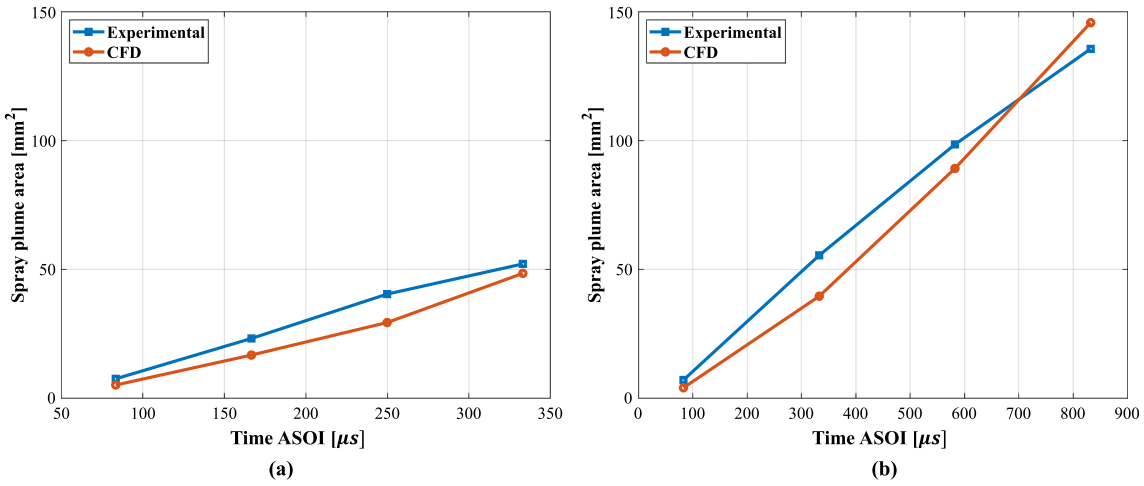

Fig. 13. Comparison of projected spray plume area between experimental and simulated tests for an ET = 350 (a) and for an ET = 600 (b) for an injection pressure of 700 bar and a back pressure of 8.4 bar.μsμs.

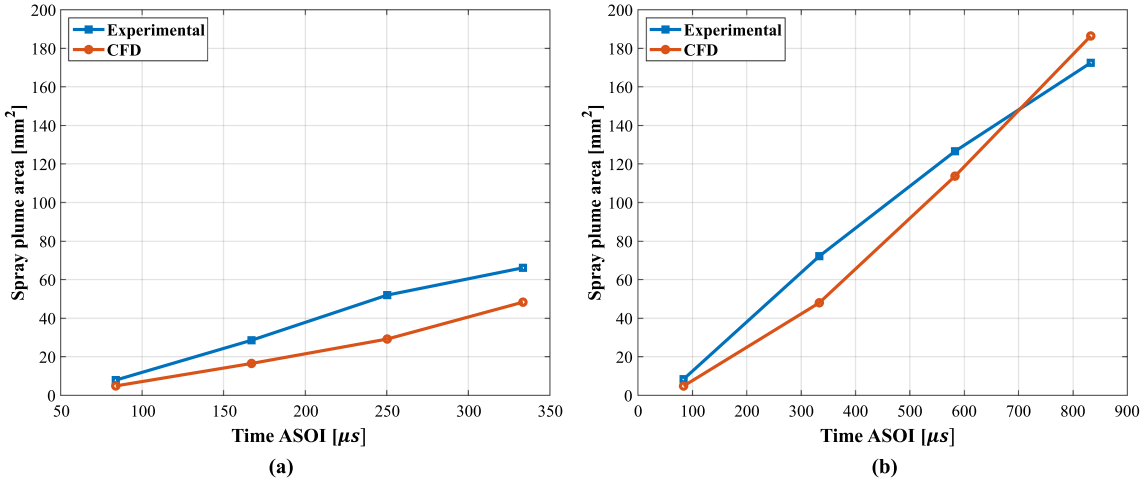

Fig. 14. Comparison of projected spray plume area between experimental and simulated tests for ET = 350 μs (a) and ET = 600 μs (b) for the injection pressure of 700 bar and the back pressure of 5 bar.

the LLP, this has been implemented also for all the other conditions listed in Table 5. Fig. 11 highlights the penetration obtained with the same injection pressure and ET of the ones of Fig. 10, but with a reduced back pressure (5 bar). Also in this case, a variable discharge coefficient (C_d = 0.92) has been adopted. Results of the comparison between the experimental and simulated LLP for the other test conditions can be found in Appendix A.

Regarding the Experimental LLP shown in both Fig. 10 and in Appendix A, the deviation of the LLP of each plume is quite pronounced during the early development of the injection. This is also evidenced in the first column of Fig. 5. Moreover, the deviation from the mean value increases as both the injection pressure and ET decreases, since the injection operative point is more subjected to ballistic phenomena.

In the contrary, for almost all the conditions, the simulated LLP during the late phase of the injection slightly show an overestimation with respect to the experiments. This is also highlighted in Fig. 12, which shows the Root Mean Square Error (RMSE) between the experimental and simulated LLPs compared during the transient opening and steady-state phases.

The adoption of a variable C_d allows to reduce the RMSE especially during the transient opening phase. Instead, during the steady-state phase, the RMSE is almost the same adopting one or the other approach. Moreover, as the injection pressure increases, the RMSE of LLP during the steady-state phase reduces. In fact, the higher is the injection pressure increases, weaker is the effect of the injector ballistic phenomena. Since the simulated spray plumes are independent from the uncertainties linked to stochastic injector dynamics, which is indeed typical of real operations, moving towards more repeatable injection operations helps reducing the discrepancy between experimental and numerical simulations.

4.2. Projected area and plume morphology

A dedicated MATLAB code has been implemented to automatically calculate the projected area of the experimental and simulated plumes starting from the generation of the contour lines. The time interval used to compare both results depends on the actual ET to be analysed. In fact, the intensity of the scattered light from the liquid droplets illuminated by the high-power lamp is directly proportional to the local density of the liquid. Hence, for times greater than the End Of Injection (EOI), the liquid phase starts to be more dispersed due to the lack of momentum provided by the injection pressure Itself. Consequently, the scattered light would be less intense for times after the EOI. Moreover, the light coming from the high-power lamp is synchronized to allow its maximum intensity to be around the middle of the injection event. This additional consideration also affects the low intensity of the scattered light during

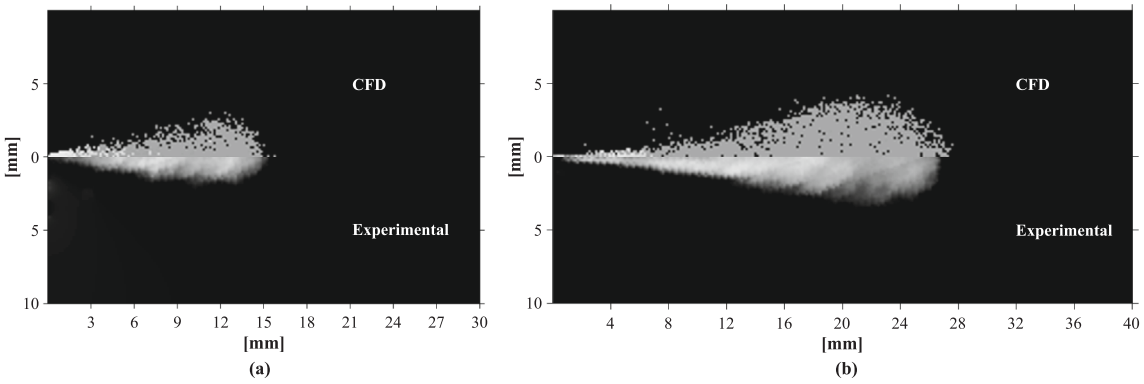

Fig. 15. Comparison of spray morphology between experimental and simulated tests for an injection pressure of 700 bar and a back pressure of 8.4 bar. ET = 350 at t = 300 aSOI (a); ET = 600 at t = 700 aSOI (b).μsμsμsμs.

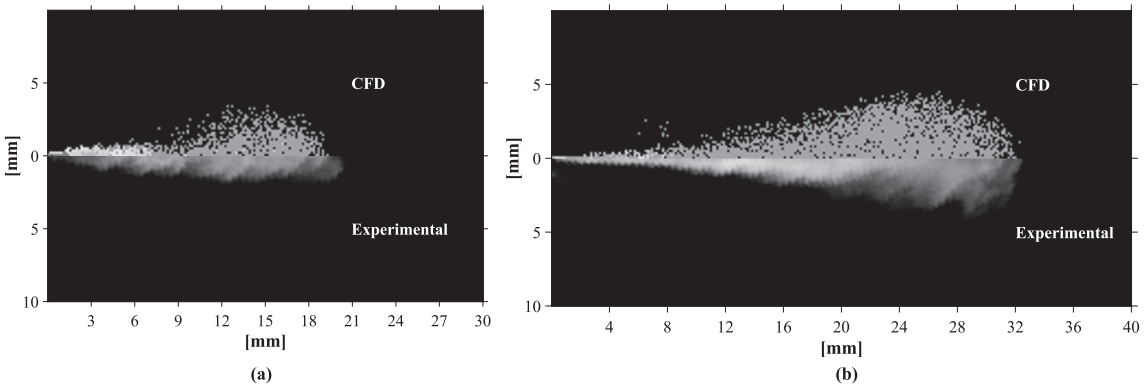

Fig. 16. Comparison of spray morphology between experimental and simulated tests for the injection pressure of 700 bar and the back pressure of 5 bar. ET = 350 μs at t = 300 μs aSOI (a); ET = 600 μs at t = 700 μs aSOI (b).

the EOI.

Fig. 13 compares the projected spray plume area between experimental and simulated tests for ET = 350 μs (a) and for an ET = 600 μs (b) at the injection pressure 700 bar and the equivalent back pressure 8.4 bar. The simulated results are quite promising for the generation of a reasonable spray in terms of morphology.

Similar considerations can be also addressed for Fig. 14, which shows the spray plume area for the same injection conditions, but for the back pressure of 5 bar. Since a lower back pressure is experienced by the injected plume, the protrusion if favoured with respect to the grater back pressure (Fig. 10 and Fig. 11). Consequently, the projected plume area in the case of reduced back pressure is higher than the one obtained with 8.4 bar of back pressure.

The effect of both the spray density reduction and the light intensity from the high-power lamp can be appreciated focusing on the experimental trends around the EOI of the projected area in Fig. 13, Fig. 14 and in Appendix B. In fact, as opposed to the simulated trends, the experimental projected spray plume areas reduce its derivative around the EOI for most the experimental tests.

The simulated projected plume area is almost always slightly overestimated compared to the experimental one. Coupling this consideration with the fact that the simulated and experimental LLP are comparable, the overestimation of the projected spray plume area might be given by taking into account the difference between an image from the Mie-Scattering technique and the one taken from simulations. In fact, the image provided by the simulation makes all the liquid droplets visible independently from the spray density and the light source. On the contrary, the experimental image might be affected by those considerations. Consequently, the contour line in the experimental images will be influenced accordingly.

The promising trend of Fig. 13 related to the spray morphology is reflected also by directly comparing the spray plume structure in the same conditions, as Fig. 15 and Fig. 16 highlight. In particular, the figures relate the experimental and simulated results in the case of a fully-developed spray plume (for ET = 350 μs, at t = 300 μs aSOI: (a); for ET = 600 μs, at t = 700 μs aSOI: (b)), for a back pressure of 8.4 and 5 bar, respectively. Since a single spray plume has been simulated, the experimental one has been chosen referring to the one that provided the lower deviation of LLP from the mean value.

The remaining results of the comparison between the experimental and simulated projected plume area and morphology for the other test conditions of Table 5 can be found in Appendix B and Appendix C, respectively.

The model introduced in this paper leads to efficiently reproduce unconventional gasoline spray injection events. The adoption of a variable C_d allows the simulated spray to match the experimental results in terms of LLP, projected area and morphology. Consequently, in the view of simulating the spray evolution inside an ICE running with GCI combustion, the tailored developed 3D-CFD code would improve the predicted distribution of the fuel inside the combustion chamber, owing to a more reasonable mixture generation before the combustion event occurring. Moreover, a precise prediction of the spray morphology will be beneficial as in indication of the regions in which the vaporized fuel will mix with the air, owing to the correct generation of the stratified mixture for a GCI concept.

5. Conclusions and future works

The research presented in this manuscript focused on the development of a tailored code to predict the behaviour of a gasoline spray

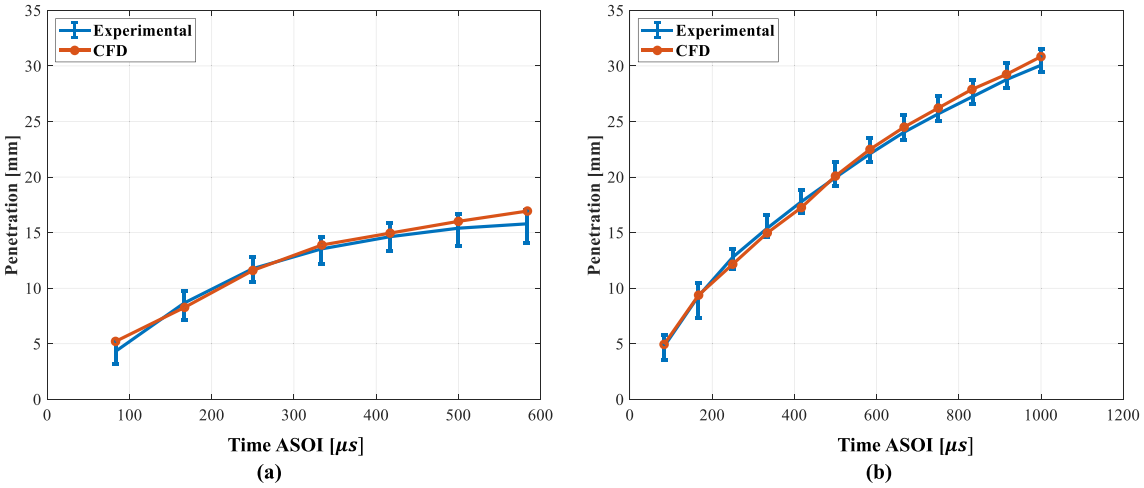

Fig. 17. Comparison of LLP between experimental and simulated tests for ET = 350 μs (a) and ET = 600 μs (b) for the injection pressure of 500 bar and the back pressure of 8.4 bar.

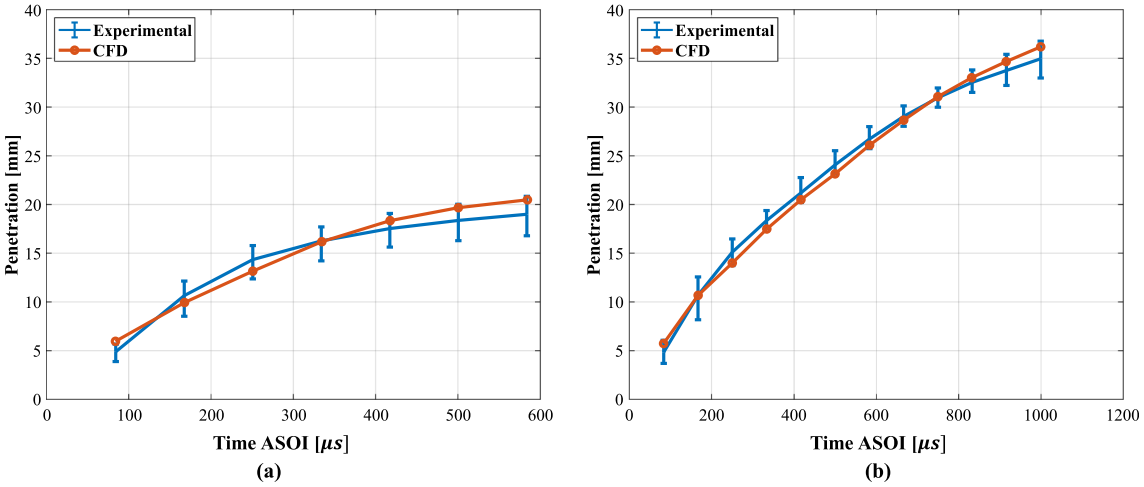

Fig. 18. Comparison of LLP between experimental and simulated tests for ET = 350 μs (a) and ET = 600 μs (b) for the injection pressure of 500 bar and the back pressure of 5 bar.

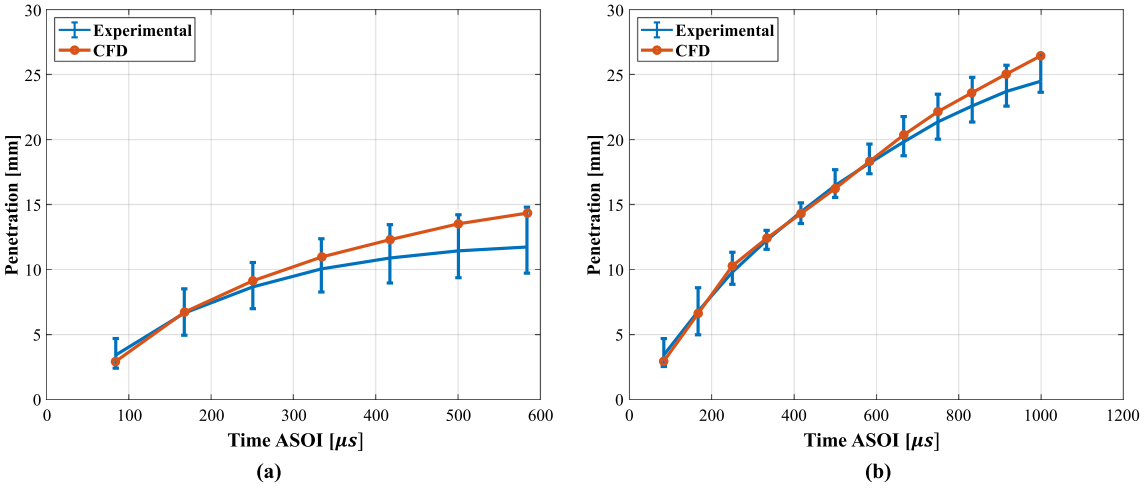

Fig. 19. Comparison of LLP between experimental and simulated tests for ET = 350 μs (a) and ET = 600 μs (b) for the injection pressure of 350 bar and the back pressure of 8.4 bar.

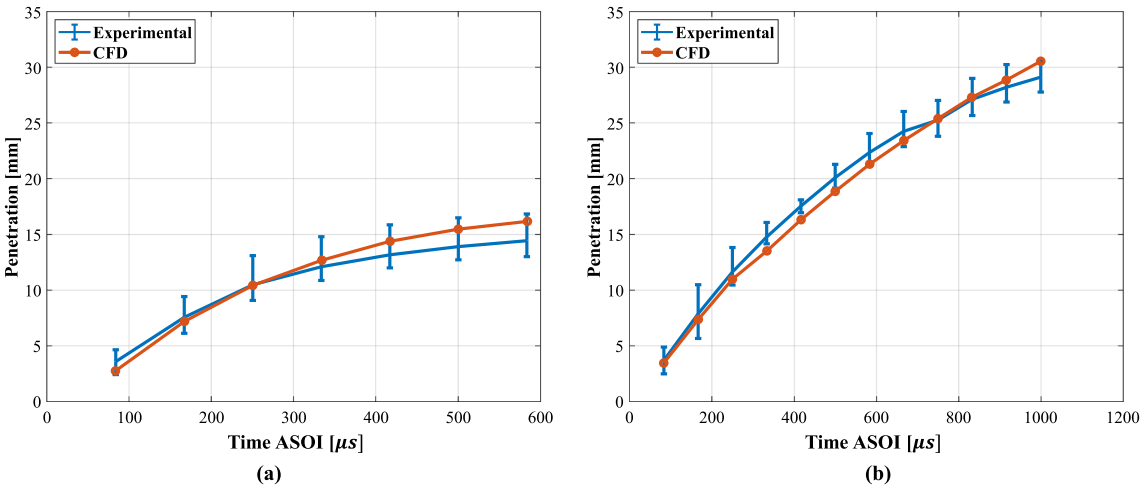

Fig. 20. Comparison of LLP between experimental and simulated tests for ET = 350 μs (a) and ET = 600 μs (b) for the injection pressure of 350 bar and the back pressure of 5 bar.

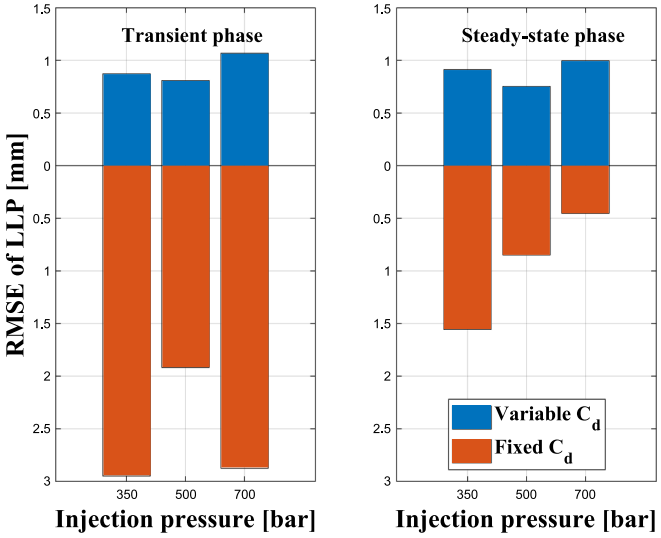

Fig. 21. Comparison of RMSE of LLP for all the tested conditions (back pressure 5 bar).

injected by a Common Rail system specifically mounted in a CDE to run in GCI mode. Spray vessel experimental tests conducted in the STEMS-CNR laboratory provided the mass flow rate and spray evolution in various conditions of injection pressure, ET and back pressure, the goal being to capture the LLP, spray plume area and morphology during 3D-CFD simulations.

Experimental data of the spray evolution obtained with the Mie-Scattering technique highlighted a strong anisotropy on the spray plumes morphology during the transient injection development. Conversely, during the steady-state phase, the morphology of each plume is almost the same.

Given the low ET used for the GCI combustion for the early injections, the tailored code considered also the transient opening dynamics in the overall simulated spray evolution. In particular, the transient opening dynamics reflected in a different reduced C_d with respect to the one calculated for longer ET at steady-state conditions.

Compared to the experimental results, the use of a fixed C_d leads to the underestimation of the simulated LLP whilst adopting the variable discharge coefficient strategy allows increased accuracy in simulating the LLP. It is underlined that the implementation of the variable discharge coefficient strategy does not require any significant additional computational effort. Regarding the projected spray plume area and morphology, the simulated results are comparable with the ones given

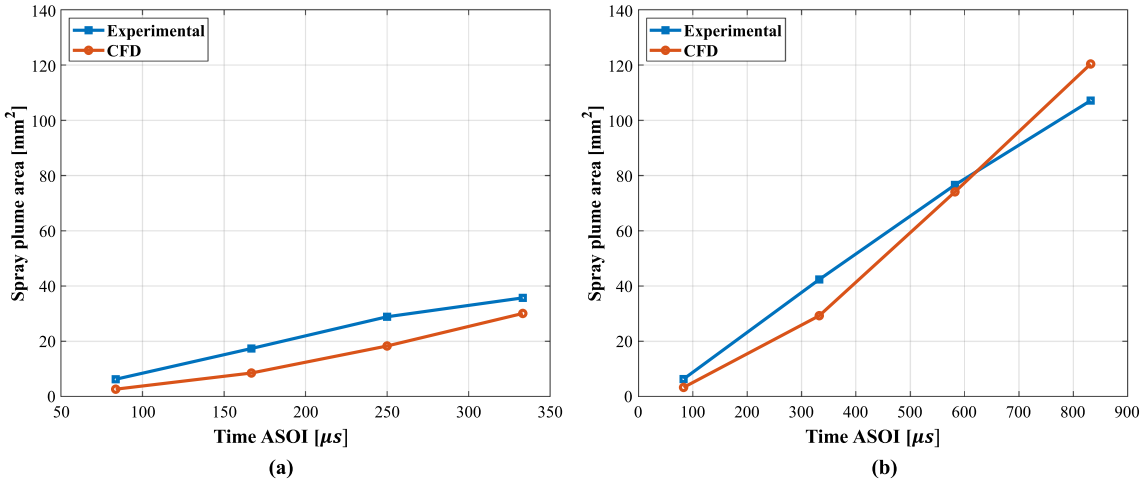

Fig. 22. Comparison of projected spray plume area between experimental and simulated tests for ET = 350 μs (a) and ET = 600 μs (b) for the injection pressure of 500 bar and the back pressure of 8.4 bar.

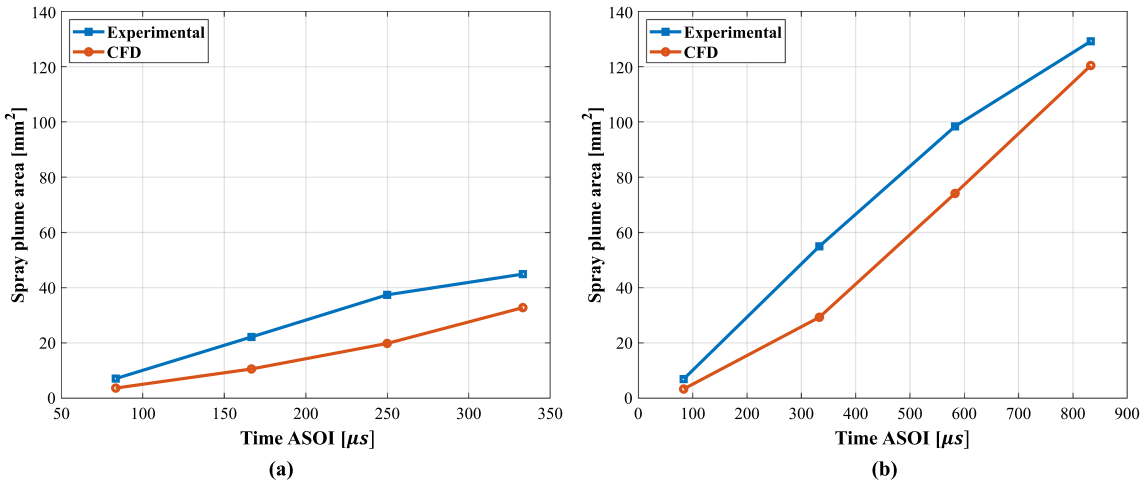

Fig. 23. Comparison of projected spray plume area between experimental and simulated tests for ET = 350 μs (a) and ET = 600 μs (b) for the injection pressure of 500 bar and the back pressure of 5 bar.

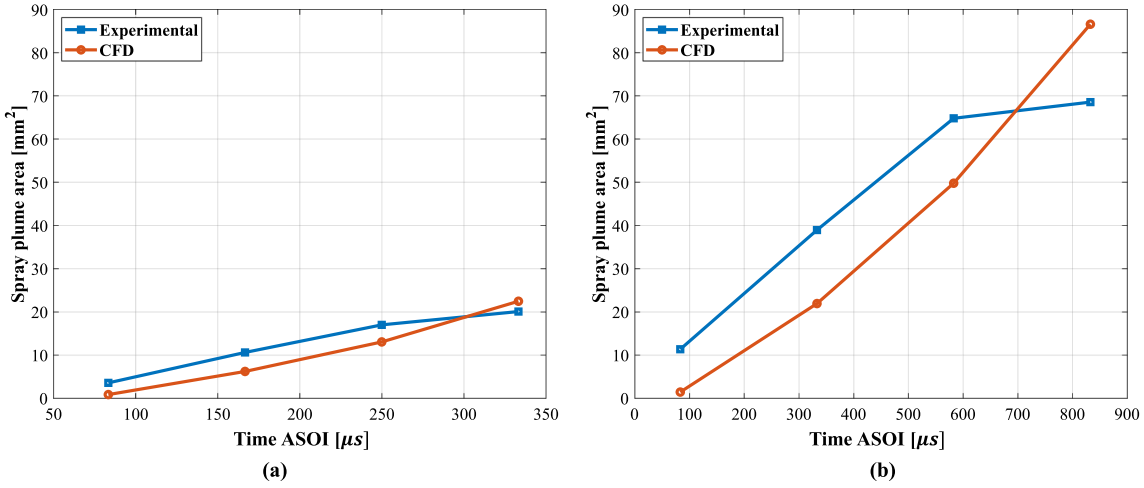

Fig. 24. Comparison of projected spray plume area between experimental and simulated tests for ET = 350 μs (a) and ET = 600 μs (b) for the injection pressure of 350 bar and the back pressure of 8.4 bar.

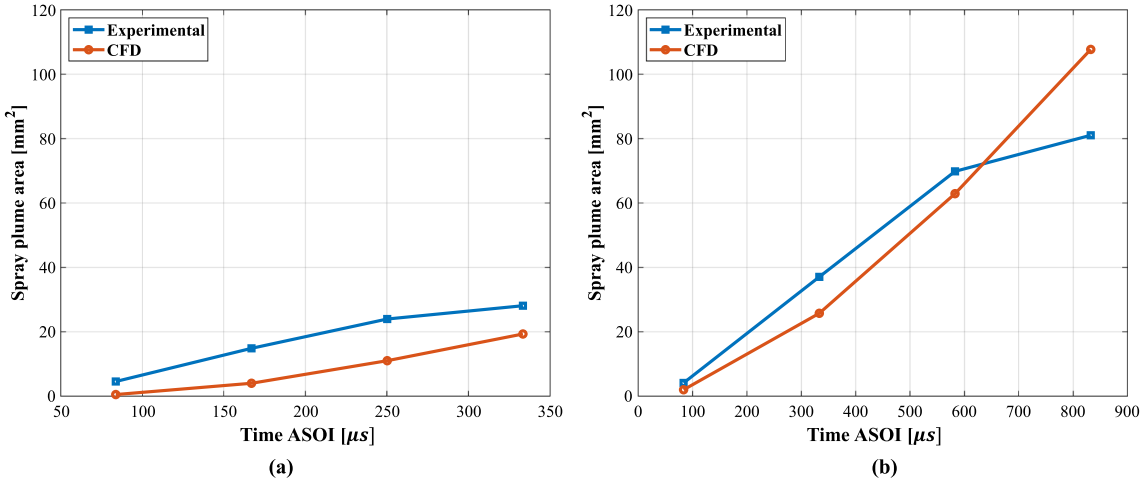

Fig. 25. Comparison of projected spray plume area between experimental and simulated tests for ET = 350 μs (a) and ET = 600 μs (b) for the injection pressure of 350 bar and the back pressure of 5 bar.

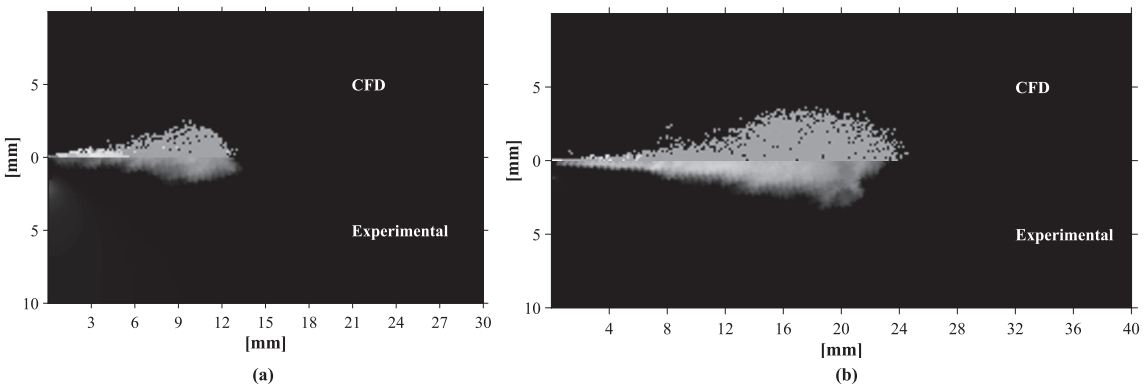

Fig. 26. Comparison of spray morphology between experimental and simulated tests for the injection pressure of 500 bar and the back pressure of 8.4 bar. ET = 350 μs at t = 300 μs aSOI (a); ET = 600 μs at t = 700 μs aSOI (b).

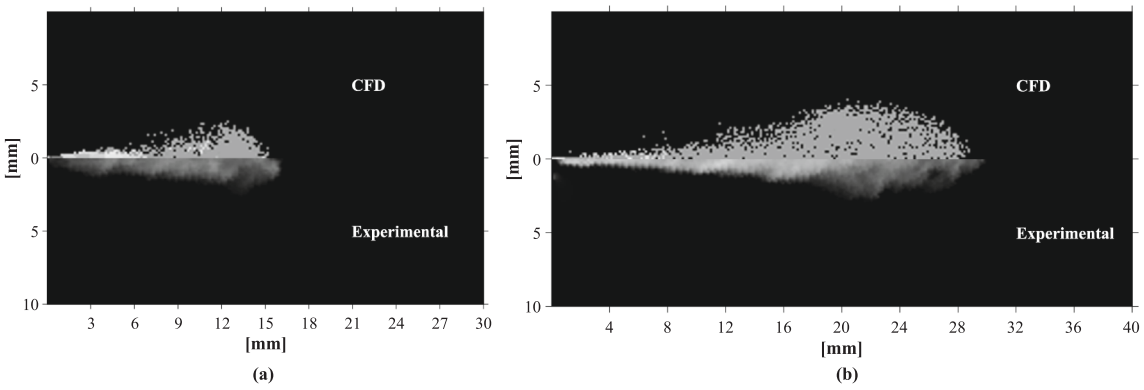

Fig. 27. Comparison of spray morphology between experimental and simulated tests for the injection pressure of 500 bar and the back pressure of 5 bar. ET = 350 μs at t = 300 μs aSOI (a); ET = 600 μs at t = 700 μs aSOI (b).

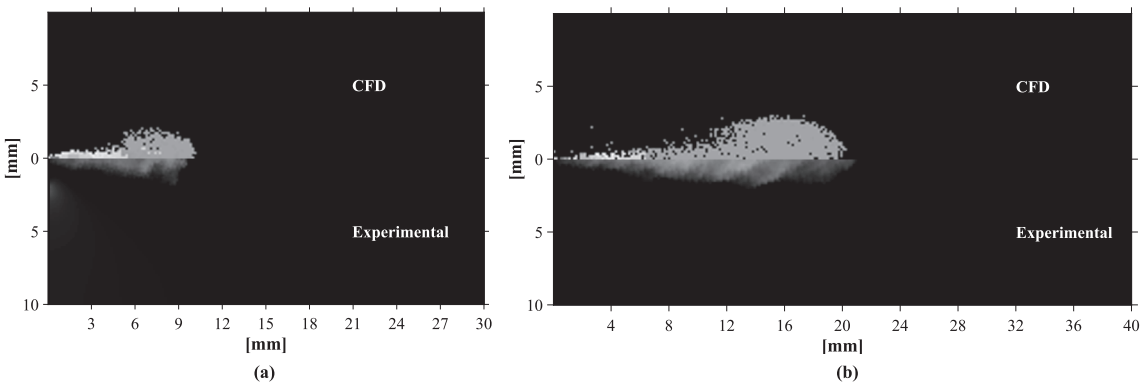

Fig. 28. Comparison of spray morphology between experimental and simulated tests for the injection pressure of 350 bar and the back pressure of 8.4 bar. ET = 350 μs at t = 300 μs aSOI (a); ET = 600 μs at t = 700 μs aSOI (b).

by the experiments.

Future studies will regard the implementation of the current code in the view of obtaining reasonable conditions to simulate the mixture generation and distribution in a combustion chamber of a CDE running in GCI mode.

CRediT authorship contribution statement

Davide Viscione: Data Curation, Validation, Formal Analysis, Investigation, Methodology, Visualization, Software, Writing – original draft, Writing – review & editing. **Valerio Mariani:** Formal analysis, Investigation, Methodology, Software, Validation, Visualization, Writing – original draft, Writing – review & editing. **Stefania Falfari:** Methodology, Visualization, Supervision, Software, Writing – review & editing. **Gian Marco Bianchi:** Methodology, Software, Supervision, Writing – review & editing. **Vittorio Ravaglioli:** Methodology, Supervision, Writing – review & editing. **Giacomo Silvagni:** Methodology, Supervision, Writing – review & editing. **Alessandro Montanaro:** Data curation, Formal analysis, Investigation, Methodology, Resources, Software, Validation, Visualization, Writing – original draft. **Luigi Allocca:** Data Curation, Validation, Formal Analysis, Investigation, Methodology, Visualization, Writing – original draft, Software, Resources.

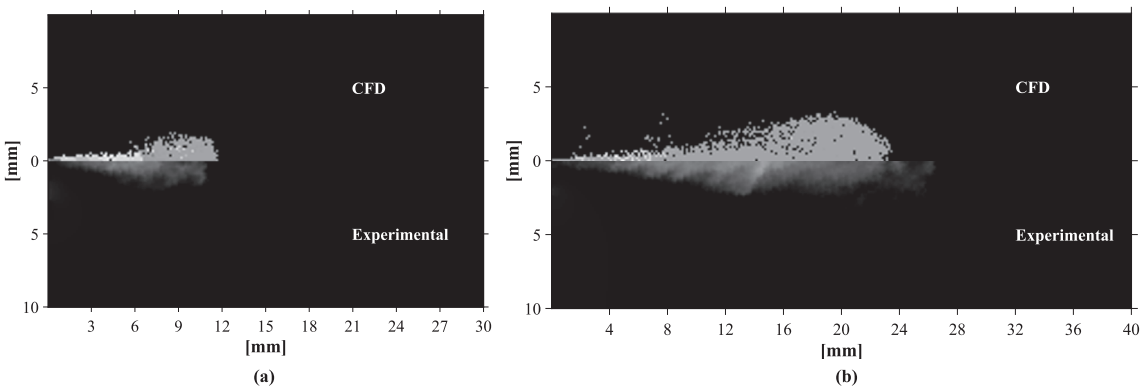

Fig. 29. Comparison of spray morphology between experimental and simulated tests for the injection pressure of 350 bar and the back pressure of 5 bar. ET = 350 μs at t = 300 μs aSOI (a); ET = 600 μs at t = 700 μs aSOI (b).

Declaration of Competing Interest

The authors declare that they have no known competing financial interests or personal relationships that could have appeared to influence the work reported in this paper.

Data availability

Data will be made available on request.

Appendix A

In this section the comparisons between the experimental and numerical LLP calculations are highlighted for the other conditions listed in Table 5 (See Figs. 17–21).

Appendix B

This section shows the comparisons between the experimental and numerical projected spray plume area calculations for the other conditions listed in Table 5 (See Figs. 22–25).

Appendix C

This section shows the comparisons between the experimental and numerical spray plume morphology for the other conditions listed in Table 5 (See Figs. 26–29).

References

[1] Lee Z, Kim T, Park S, Park S. Review on spray, combustion, and emission characteristics of recent developed direct-injection spark ignition (DISI) engine system with multi-hole type injector. Fuel Jan. 2020;259:116209. https://doi.org/10.1016/j.fuel.2019.116209.
[2] Naik GG, Dharmadhikari HM. Methods for reducing NOx and PM emissions in compression ignition engine: A review. Mater Today Proc 2023;72:1406–12. https://doi.org/10.1016/j.matpr.2022.09.339.
[3] Krishnamoorthi M, Malayalamurthi R, He Z, Kandasamy S. A review on low temperature combustion engines: performance, combustion and emission characteristics. Renew Sustain Energy Rev Dec. 2019;116:109404. https://doi.org/10.1016/j.rser.2019.109404.
[4] H. Zhao, J. Li, T. Ma, and N. Ladommatos, 'Performance and Analysis of a 4-Stroke Multi-Cylinder Gasoline Engine with CAI Combustion', presented at the SAE 2002 World Congress & Exhibition, Mar. 2002, pp. 2002-01–0420. doi: 10.4271/2002-01-0420.
[5] Sellnau MC, Sinnamon J, Hoyer K, Husted H. Full-Time Gasoline Direct-Injection Compression Ignition (GDCI) for High Efficiency and Low NOx and PM. SAE Int J Engines Apr. 2012;5(2):300–14. https://doi.org/10.4271/2012-01-0384.
[6] Sjöberg. M, Dec. J. E, Cernansky N. P. 'Potential of Thermal Stratification and Combustion Retard for Reducing Pressure-Rise Rates in HCCI Engines, Based on Multi-Zone Modeling and Experiments', presented at the SAE 2005 World Congress & Exhibition, Apr. 2005, pp. 2005-01–0113. doi: 10.4271/2005-01-0113.
[7] Sjöberg, M. Dec, J. E. 'Smoothing HCCI Heat-Release Rates Using Partial Fuel Stratification with Two-Stage Ignition Fuels', presented at the SAE 2006 World Congress & Exhibition, Apr. 2006, pp. 2006-01–0629. doi: 10.4271/2006-01-0629.
[8] Dempsey AB, Curran SJ, Wagner RM. A perspective on the range of gasoline compression ignition combustion strategies for high engine efficiency and low NOx and soot emissions: effects of in-cylinder fuel stratification. Int J Engine Res Oct. 2016;17(8):897–917. https://doi.org/10.1177/1468087415621805.
[9] Atef N, Badra J, Jaasim M, Im HG, Sarathy SM. Numerical investigation of injector geometry effects on fuel stratification in a GCI engine. Fuel Feb. 2018;214:580–9. https://doi.org/10.1016/j.fuel.2017.11.036.
[10] Priyadarshini P, Sofianopoulos A, Mamalis S, Lawler B, Lopez-Pintor D, Dec JE. Understanding partial fuel stratification for low temperature gasoline combustion using large eddy simulations. Int J Engine Res Jun. 2021;22(6):1872–87. https://doi.org/10.1177/1468087420921042.
[11] Agarwal AK, Solanki VS, Krishnamoorthi M. Gasoline compression ignition (GCI) combustion in a light-duty engine using double injection strategy. Appl Therm Eng Mar. 2023;223:120006. https://doi.org/10.1016/j.applthermaleng.2023.120006.
[12] Cung K. *et al.*, 'Investigation of Gasoline Compression Ignition (GCI) Combustion in a High Compression-Ratio Heavy-duty Single-Cylinder Diesel Engine', presented at the SAE WCX Digital Summit, Apr. 2021, pp. 2021-01–0495. doi: 10.4271/2021-01-0495.
[13] Curran S, Szybist J, Kaul B, Easter J, Sluder S. 'Fuel stratification effects on gasoline compression ignition with a regular-grade gasoline on a single-cylinder medium-duty diesel engine at low load'. SAE Int J Adv Curr Pract Mobil Sep. 2021;4(2):488–501. https://doi.org/10.4271/2021-01-1173.
[14] Park SH, Youn IM, Lim Y, Lee CS. Influence of the mixture of gasoline and diesel fuels on droplet atomization, combustion, and exhaust emission characteristics in a compression ignition engine. Fuel Process Technol Feb. 2013;106:392–401. https://doi.org/10.1016/j.fuproc.2012.09.004.
[15] Kim K, Kim D, Jung Y, Bae C. Spray and combustion characteristics of gasoline and diesel in a direct injection compression ignition engine. Fuel Jul. 2013;109:616–26. https://doi.org/10.1016/j.fuel.2013.02.060.
[16] Feng L, et al. Gasoline spray characteristics using a high pressure common rail diesel injection system by the method of laser induced exciplex fluorescence. Fuel Oct. 2021;302:121174. https://doi.org/10.1016/j.fuel.2021.121174.
[17] Payri R, García A, Domenech V, Durrett R, Plazas AH. An experimental study of gasoline effects on injection rate, momentum flux and spray characteristics using a common rail diesel injection system. Fuel Jul. 2012;97:390–9. https://doi.org/10.1016/j.fuel.2011.11.065.
[18] Sellnau M, Foster M, Hoyer K, Moore W, Sinnamon J, Husted H. Development of a gasoline direct injection compression ignition (GDCI) engine. SAE Int J Engines Apr. 2014;7(2):835–51. https://doi.org/10.4271/2014-01-1300.
[19] Wang Y, Wang X, Pan J, Wei H, Zhou X, Pan M. Effects of different injection strategies on mixing, combustion and emission behavior of gasoline compression ignition (GCI) engines. Fuel Jun. 2022;317:123486. https://doi.org/10.1016/j.fuel.2022.123486.
[20] Zhang M, Derafshzan S, Richter M, Lundgren M. Effects of different injection strategies on ignition and combustion characteristics in an optical PPC engine. Energy Jul. 2020;203:117901. https://doi.org/10.1016/j.energy.2020.117901.
[21] Ravaglioli. V, Ponti. F, Silvagni. G, Moro. D, Stola. F, De Cesare. M, 'Performance Assessment of Gasoline PPC in a Light-Duty CI Engine', presented at the WCX SAE World Congress Experience, Mar. 2022, pp. 2022-01–0456. doi: 10.4271/2022-01-0456.
[22] Stola. F, Ravaglioli. V, Silvagni. G, Ponti. F, De Cesare. M, 'Injection Pattern Investigation for Gasoline Partially Premixed Combustion Analysis', presented at the 14th International Conference on Engines & Vehicles, Sep. 2019, pp. 2019-24–0112. doi: 10.4271/2019-24-0112.
[23] F. Stola, V. Ravaglioli, G. Silvagni, F. Ponti, and M. De Cesare, 'Analysis of the Effects of Injection Pressure Variation in Gasoline Partially Premixed Combustion', presented at the SAE WCX Digital Summit, Apr. 2021, pp. 2021-01–0517. doi: 10.4271/2021-01-0517.

[24] Ra Y, Yun JE, Reitz RD. Numerical parametric study of diesel engine operation with gasoline. Combust Sci Technol Jan. 2009;181(2):350–78. https://doi.org/10.1080/00102200802504665.
[25] Cho. K, Zhang. Y, Sellnau. M, 'Investigation on Combining Partially Premixed Compression Ignition and Diffusion Combustion for Gasoline Compression Ignition—Part 1: Fuel Reactivity and Injection Strategy Effects', *SAE Int. J. Sustain. Transp. Energy Environ. Policy*, vol. 2, no. 1, pp. 13-02-01–0003, Mar. 2021, doi: 10.4271/13-02-01-0003.
[26] Moiz. A. A, Cung. K, Briggs. T, Bitsis. D. C, 'Investigation of Gasoline Compression Ignition in a Heavy-Duty Diesel Engine Using Computational Fluid Dynamics', presented at the SAE WCX Digital Summit, Apr. 2021, pp. 2021-01–0493. doi: 10.4271/2021-01-0493.
[27] Piano A, Millo F, Postrioti L, Biscontini G, Cavicchi A, Pesce FC. Numerical and experimental assessment of a solenoid common-rail injector operation with advanced injection strategies. SAE Int J Engines Apr. 2016;9(1):565–75. https://doi.org/10.4271/2016-01-0563.
[28] Payri R, Gimeno J, Venegas O, Plazas-Torres AH. Experimental and computational study of the influence of partial needle lift on nozzle flowin diesel fuel injectors. At Sprays 2012;22(8):687–714. https://doi.org/10.1615/AtomizSpr.2012005810.
[29] Payri. R, Gimeno. J, Venegas. O, Plazas. A. H, 'Effect of Partial Needle Lift on the Nozzle Flow in Diesel Fuel Injectors', presented at the SAE International Powertrains, Fuels and Lubricants Meeting, Aug. 2011, pp. 2011-01–1827. doi: 10.4271/2011-01-1827.
[30] Bianchi. G. M, Falfari. S, Parotto. M, Osbat. G, 'Advanced Modeling of Common Rail Injector Dynamics and Comparison with Experiments', presented at the SAE 2003 World Congress & Exhibition, Mar. 2003, pp. 2003-01–0006. doi: 10.4271/2003-01-0006.
[31] Desantes. J. M, Arrègle. J, Rodríguez. P. J, 'Computational Model for Simulation of Diesel Injection Systems', presented at the International Congress & Exposition, Mar. 1999, pp. 1999-01–0915. doi: 10.4271/1999-01-0915.
[32] Catania AE, Dongiovanni C, Mittica A, Badami M, Lovisolo F. Numerical analysis versus experimental investigation of a distributor-type diesel fuel-injection system. J Eng Gas Turbines Power Oct. 1994;116(4):814–30. https://doi.org/10.1115/1.2906890.
[33] Cantore. G, Mattarelli. E, Boretti. A. A, 'Experimental and Theoretical Analysis of a Diesel Fuel Injection System', presented at the International Congress & Exposition, Mar. 1999, pp. 1999-01–0199. doi: 10.4271/1999-01-0199.
[34] Coppo M, Dongiovanni C, Negri C. Numerical analysis and experimental investigation of a common rail-type diesel injector. J Eng Gas Turbines Power Oct. 2004;126(4):874–85. https://doi.org/10.1115/1.1787502.
[35] Yamaguchi. A, Koopmans L, Helmantel A, Karrholm F. P, Dahlander P, 'Spray Characterization of Gasoline Direct Injection Sprays Under Fuel Injection Pressures up to 150 MPa with Different Nozzle Geometries', presented at the International Powertrains, Fuels & Lubricants Meeting, Jan. 2019, pp. 2019-01–0063. doi: 10.4271/2019-01-0063.
[36] Payri R, Garcia A, Domenech V, Durrett R, Plazas A Torres, 'Hydraulic Behavior and Spray Characteristics of a Common Rail Diesel Injection System Using Gasoline Fuel', presented at the SAE 2012 World Congress & Exhibition, Apr. 2012, pp. 2012-01–0458. doi: 10.4271/2012-01-0458.
[37] Bosch W, 'The Fuel Rate Indicator: a New Measuring Instrument For Display of the Characteristics of Individual Injection', presented at the National Powerplant and Transportation Meetings, Feb. 1966, p. 660749. doi: 10.4271/660749.
[38] Allocca L, Montanaro A, Cipolla G, Vassallo A, 'Spatial-Temporal Characterization of Alternative Fuel Sprays from a Second-Generation Common-Rail Fuel Injection System for Euro4 Passenger Car Application', presented at the Powertrains, Fuels and Lubricants Meeting, Jun. 2009, pp. 2009-01–1856. doi: 10.4271/2009-01-1856.
[39] Montanaro A, Allocca L, 'Impact of the Nozzle Coking on Spray Formation for Diesel Injectors', presented at the SAE/KSAE 2013 International Powertrains, Fuels & Lubricants Meeting, Oct. 2013, pp. 2013-01–2546. doi: 10.4271/2013-01-2546.
[40] Montanaro A, Allocca L, Lazzaro M, 'Iso-Octane Spray from a GDI Multi-Hole Injector under Non- and Flash Boiling Conditions', presented at the International Powertrains, Fuels & Lubricants Meeting, Oct. 2017, pp. 2017-01–2319. doi: 10.4271/2017-01-2319.
[41] Brusiani F, Bianchi G. M, Falfari S, Onorati A, Lucchini T, Di Gioia R, 'Influence of Cylindrical, k, and ks Diesel Nozzle Shape on the Injector Internal Flow Field and on the Emerging Spray Characteristics', presented at the SAE 2014 World Congress & Exhibition, Apr. 2014, pp. 2014-01–1428. doi: 10.4271/2014-01-1428.
[42] Reitz R. D, Diwakar R, 'Effect of Drop Breakup on Fuel Sprays', presented at the SAE International Congress and Exposition, Feb. 1986, p. 860469. doi: 10.4271/860469.